Article:
Peng, Z, Nan, J, Zhang, L et al. (6 more authors) (2023) Evidence for abundant organic matter in a Neoarchean banded iron formation. American Mineralogist, 108 (12). ISSN 0003-004X

https://doi.org/10.2138/am-2023-8927

Revision 1

Evidence for abundant organic matter in a Neoarchean banded iron formation

Zidong Peng[a, b, *], Jingbo Nan[c, d], Lianchang Zhang[a, b, e], Simon W. Poulton[f], Junlie Zhou[g], Yuan Yuan[h, b], Kaiwen Ta[i], Changle Wang[a, b, e, *], Mingguo Zhai[a, b, e]

a Key Laboratory of Mineral Resources, Institute of Geology and Geophysics, Chinese Academy of Sciences, Beijing 100029, China

b Innovation Academy for Earth Science, Chinese Academy of Sciences, Beijing 100029, China

c Department of Ocean Science and Engineering, Southern University of Science and Technology, Shenzhen 518055, China

d Center for High Pressure Science and Technology Advanced Research (HPSTAR), Beijing 100094, China

e University of Chinese Academy of Sciences, Beijing 100049, China

f School of Earth and Environment, University of Leeds, Leeds, LS2 9JT, UK

g School of Environment & Resource, Xichang University, Xichang 615000, China

h Key Laboratory of Shale Gas and Geoengineering, Institute of Geology and Geophysics, Chinese Academy of Sciences, Beijing 100029, China

i Institute of Deep Sea Science and Engineering, Chinese Academy of Sciences, Sanya 572000, China

* Corresponding author: pengzidong2007@126.com; wangcl@mail.iggcas.ac.cn

ABSTRACT

Microbial Fe(II) oxidation has been proposed as a major source of Fe minerals during deposition of banded iron formations (BIFs) in the Archean and Proterozoic Eons. The conspicuous absence of organic matter (OM) or graphitic carbon from BIFs, however, has given rise to divergent views on the importance of such a biologically-mediated iron cycle. Here, we present mineral associations, major element concentrations, total carbon contents and carbon isotope compositions for a set of lower amphibolite-facies BIF samples from the Neoarchean Zhalanzhangzi BIF in the

Qinglonghe supracrustal sequence, Eastern Hebei, China. Graphite grains with crystallization temperatures (~470°C) that are comparable to that predicted for the regional metamorphic grade are widely distributed, despite highly variable iron (12.9 to 54.0wt%) and total organic carbon (0.19 to 1.10wt%) contents. The crystalline graphite is interpreted to represent the metamorphosed product of syngenetic biomass, based on its co-occurrence with apatite rosettes and negative bulk rock $\delta^{13}C_{organic}$ values (-23.8 to -15.4‰). Moreover, the crystalline graphite is unevenly distributed between iron- and silica-rich bands. In the iron-rich bands, abundant graphite relicts are closely associated with magnetite and/or are preserved within carbonate minerals (i.e., siderite, ankerite and calcite) with highly negative bulk rock $\delta^{13}C_{carb}$ values (-16.73 to -6.33‰), indicating incomplete reduction of primary ferric (oxyhydr)oxides by OM. By comparison, only minor graphite grains are observed in the silica-rich bands. Normally, these grains are preserved within quartz or silicate minerals and thus did not undergo oxidation by Fe(III). In addition, the close association of graphite with iron-bearing phases indicates that ferric (oxyhydr)oxides may have exerted a first order control on the abundance of OM. Combined, the biological oxidation of Fe(II) in the oceanic photic zone and subsequent burial of ferric (oxyhydr)oxides and biomass in sediments to form BIFs, suggests that a BIF-dependent carbon cycle was important in the Archean Eon. Although significant re-adsorption of phosphorus to ferric (oxyhydr)oxides and the formation of authigenic phosphate minerals at the sediment-water interface would be expected, oxidation of biomass in BIFs may have recycled at least a portion of the P (and other nutrients) released from reactions between OM and ferric (oxyhydr)oxides to the overlying water column, potentially promoting further primary productivity.

Keywords: Organic matter, Carbon isotopes, Apatite, Raman spectroscopy, Banded iron formation, Neoarchean.

INTRODUCTION

Banded iron formations (BIFs) are layered, iron-rich and siliceous chemical sediments that formed predominantly through the precipitation of ferric iron [Fe(III) (oxyhydr)oxide] in Archean and Paleoproterozoic ferruginous oceans (e.g., Bekker et al., 2014; Konhauser et al., 2017; Mänd et al., 2021). Although it remains possible that photochemical Fe(II) oxidation may have contributed to BIF deposition (e.g., Konhauser et al., 2007; Pecoits et al., 2015; Nie et al., 2017), biologically

assisted Fe(II) oxidation, either directly through photoferrotrophy or indirectly through oxygenic photosynthesis, is generally favored (Cloud, 1973; Konhauser et al., 2002; Kappler and Newman, 2004; Planavsky et al., 2009; Czaja et al., 2013). If so, BIFs likely record the activity of Earth's early photosynthetic biosphere, and the oxidation of Fe(II) would thus be expected to produce biomass that settled to the seafloor together with the Fe(III) minerals (e.g., Posth et al., 2010; Konhauser et al., 2011).

Studies to date, paradoxically, reveal a low content of organic matter (OM), or graphitic carbon as its metamorphosed equivalent, in BIFs, with total organic carbon (TOC) contents typically lower than 0.5 wt% (e.g., Gole and Klein, 1981; Klein, 2005; Heimann et al., 2010; Tong et al., 2021). This means that OM may have been oxidized either by the combined metabolic processes of fermentation and chemoheterotrophy during diagenesis (Konhauser et al., 2005), or abiotically during subsequent metamorphism (Van Zuilen et al., 2002). Significantly, coupling the oxidation of OM to the reduction of part of the Fe(III) mineral pool not only provides an explanation for the low TOC content of BIFs, but may also explain the presence of Fe(II)-bearing minerals (magnetite, siderite and greenalite) (Li et al., 2013; Konhauser et al., 2017), highly negative $\delta^{13}C$ values of Fe(II)-rich carbonates (Heimann et al., 2010; Craddock and Dauphas, 2011), and negative $\delta^{56}Fe$ values for some magnetite and/or siderite (Johnson et al., 2008; Heimann et al., 2010) in BIFs. Alternatively, the conspicuous absence of photosynthetic biomass produced from biological Fe(II) oxidation during BIF formation could be the result of a combination of the physical separation of biomass from Fe(III) by-products during iron deposition, and the oxidation of limited OM by Fe(III) after burial. Experiments and modeling (Thompson et al., 2019) have revealed that in the presence of high silica ($\geq$ 1 mM; Jones et al., 2015), which would be expected for Precambrian seawater (Siever, 1992), pelagic photoferrotrophs are particularly capable of avoiding co-sedimentation with Fe(III), and thus remain buoyant with the potential for separation of biomass from Fe(III) at a large scale. As a result, the excess biomass would have instead deposited in shales, where it likely fueled methanogenesis once reactive Fe(III) minerals had been reduced. Ultimately, this would have resulted in a significant flux of methane to the atmosphere, while the small fraction of biomass that co-precipitated with Fe(III) would have fueled the diagenetic formation of reduced Fe(II) phases in BIFs (Thompson et al., 2019).

By contrast to the above high bio-productivity hypothesis, the low TOC content in BIFs has also been interpreted as the result of minimal biomass production during BIF deposition. Considering that

clay minerals have the capability to protect OM from being oxidized (e.g., Kennedy et al., 2014; McMahon et al., 2016; Playter et al., 2017), Dodd et al. (2019a) compared the OM-clay associations in BIFs and associated metapelites ranging in ages from 3.7 to 1.8 Ga. This reveals that clays in both BIFs and metapelites show little difference in their ability to bind OM, and that in the pelite samples around 80-95% of the observable OM occurs with or within phyllosilicates (e.g., muscovite, chamosite and biotite), yet in the BIFs no OM was found within phyllosilicates (including grunerite, actinolite, minnesotaite and stilpnomelane). Given such constraints, Dodd et al. (2019a) conclude that there may have been minimal biomass production at sites of BIF formation, implying that the deposition of OM in BIFs was much lower than previously thought. If the initial availability of OM that fueled Fe(III) mineral reduction was minimal as Dodd et al. (2019a) propose, then the deposition of BIF itself would in turn lead to a less productive water column, due to the ability of Fe(III) minerals to scavenge and sequester phosphorus and other nutrients from the seawater (e.g., Bjerrum and Canfield, 2002; Scott et al., 2013). Accordingly, this process would have caused a particularly pronounced nutrient limitation and hence a negative productivity feedback.

To investigate whether the low organic content of Precambrian BIFs is a result of near-complete oxidation of available initial biomass, or an intrinsic feature related to limited OM production during iron deposition, we document the mineral associations, major element concentrations, total carbon contents and carbon isotope compositions of a set of BIF samples with highly variable iron and TOC contents from the late Neoarchean Zhalanzhangzi BIF in the Qinglonghe supracrustal sequence, Eastern Hebei.

GEOLOGIC SETTING

Eastern Hebei is situated in the northern part of the North China Craton (NCC) (Fig. 1). The exposed strata in this area consists predominantly of early Archean to Paleoproterozoic metamorphic basement rocks that are either partially overlain by Mesoproterozoic to Mesozoic platform cover sequences or are intruded by Cenozoic granites (e.g., Geng, 1998; Nutman et al., 2011) (Fig. 1). The early Archean basement in this region is exposed in the Caozhuang area and is represented by 3.28-2.94 Ga orthogneisses and fuchsite-bearing quartzites with detrital zircon ages of 3.89-3.13 Ga (Liu et al., 1992; Wilde et al., 2008; Nutman et al., 2011). By comparison, Neoarchean rocks that comprise of 2.6-2.5 Ga plutonic gneisses and minor 2.8-2.5 Ga supracrustal rocks are more abundant

(Geng et al., 2006; Nutman et al., 2011; Guo et al., 2013), covering almost 95% of the total NCC basement exposed in Eastern Hebei. Notably, the minor Neoarchean supracrustal rocks are either interlayered with the orthogneisses or occur as rafts or sheets of variable dimensions within the plutonic gneisses (Fig. 1). They can be further divided into different groups in terms of various areas, including the Zunhua, Qianxi, Luanxian, Dantazi, Shuangshanzi and Zhuzhangzi groups (e.g., Qian et al., 1985; Zhang et al., 1986), although a consensus with respect to their relatively stratigraphic sequence has not been achieved (e.g., Sun et al., 2010; Lv et al., 2012; Liu et al., 2014).

The Qinglonghe supracrustal sequence (QSS) is located in the eastern part of Eastern Hebei (Fig. 1), and comprises the Shuangshanzi and Zhuzhangzi groups (Shen et al., 2005). In contrast to most amphibolite- to granulite-facies metamorphosed Neoarchean terranes in Eastern Hebei (Kröner et al., 1998; Zhao et al., 1998), the QSS has only experienced greenschist- to lower amphibolite-facies metamorphism related to the regional emplacement of a granite porphyry at ca. 2.50 Ga (Shen et al., 2005; Lv et al., 2012). The exposed rocks in the Shuangshanzi Group are dominated by volcanic units, including meta-mafic and -felsic volcanic rocks, and minor metapelites (Shen et al., 2005; Lv et al., 2012). By comparison, the overlying Zhuzhangzi Group comprises metaconglomerates and metapelites, as well as minor metasandstones and BIFs (Shen et al., 2005).

Zhalanzhangzi BIF of this study is preserved within the upper section of the Zhuzhangzi Group (Wan et al., 2012; Chen et al., 2015). The BIF layers normally form repeated cycles of metapelites (two mica quartz schist), BIFs and metasandstones (biotite quartz schist) (Fig. 2), and are inferred to have been deposited in a rifted basin based on a previously documented intra-continental rift setting (Lv et al., 2012) for the QSS. Zircon U-Pb dating shows that magmatic zircons from the meta-felsic volcanic rocks in the Shuangshanzi Group were crystallized at 2511 ± 12 Ma (Lv et al., 2012), representing the maximum depositional age of the BIF, while magmatic zircons from a granite-porphyry intrusion which intruded into the upper section of the Zhuzhangzi Group (i.e., the BIF-bearing sequence) have been dated at 2498 ± 8 Ma (Shen et al., 2005), constraining the minimum depositional age of the BIF. The depositional age of the Zhalanzhangzi BIF thus can be constrained between 2511 ± 12 and 2498 ± 8 Ma. The BIF samples for this study were taken from two well preserved drill cores located in the central part of the ~3.5 km long BIF-bearing sequence (Fig. S1), with drill core Zk1103 probably documenting a slightly shallower water depth relative to Zk1104 (Fig. 2).

METHODS

Sample preparation

Centimeter-sized rock chips were extracted from the internal regions of BIF samples by sawing with sterile, deionized water. Prior to cutting, the saw was treated with 5% sodium hypochlorite and then rinsed with sterile, deionized water. Twenty-six thin sections were then prepared with a final polishing step using Al_2O_3 0.5 μm power in deionized water, for subsequent investigation using optical and Raman spectroscopy. To limit laboratory contamination, no organic material was introduced during the procedure, except for the epoxy used to fix thin sections. Samples were not sputter coated before Raman spectroscopy and scanning electron microscopy analyses in order to avoid any contamination from carbon. After this stage, selected samples (see Table S1 for details) were coated with carbon for electron probe micro-analysis. Deionized water and an ultrasonic bath were used to clean the thin sections before observations. A broken rock fragment with an unexposed, fresh surface was also prepared for sample 1104d. By comparing the result of this fragment with those of the polished thin sections, we could further confirm whether any artificial organic component was introduced. In addition, approximately five-gram rock chips of fifteen representative BIF samples were crushed to powder (~200 μm) using an agate pestle and mortar for the analysis of major elements, total carbon contents and carbon isotopes. The agate mill was cleaned with deionized water and alcohol throughout the procedure.

Major elements analysis

Major element contents were determined at the ALS Chemex, Guangzhou, China, using an X-ray fluorescence spectrometer with an analytical error of less than 3%, as estimated through analyses of the GBW07105, GBW07111, and GBW07112 geostandards. Loss on ignition (LOI) was determined by heating powders at 1,000°C for 2 h and measuring the relative decrease in weight. Values for replicates (1103a-r and 1104a-r) and geological standards are provided in Table S2.

Raman spectroscopy

Raman spectroscopy was conducted on both the thin sections and the rock fragment using a WiTec alpha 300R confocal Raman spectrometer equipped with a 532 nm excitation laser, at the Institute of Deep-sea Science and Engineering, Chinese Academy of Sciences, Sanya (IDSSE). The

analysis was operated at a power less than 1 mW, to avoid graphitization of the organic matter, with integration times of 10 s. Raman spectra were collected using a 100× objective to provide a spatial resolution of around 1 μm. All Raman spectra were fitted using the Fast Fourier transform method after background subtraction with a polynomial function. Assignment of molecular vibrations is based on published data (Dodd et al., 2019a, b).

Scanning electron and energy dispersive X-ray spectroscopy analyses

Scanning electron microscopy (SEM) and energy dispersive spectroscopic (EDS) analyses were used to characterize the morphology and composition of selected targets, using a Thermoscientific Apreo C SEM equipped with an energy-dispersive X-ray spectroscope and AZtec system provided by Oxford Instruments at the IDSSE. Standard operating conditions for SEM imaging was 2 and 15 kV accelerating voltage at a working distance of 10 mm. An accelerating voltage of 15 kV was used for the X-ray analysis to obtain adequate X-ray counts.

Electron probe micro-analysis

Major element compositions of minerals were obtained using a JEOL JXA8100 electron probe microanalyzer (EPMA) at the Institute of Geology and Geophysics, Chinese Academy of Sciences, Beijing (IGGCAS). Analysis was carried out at an accelerating voltage of 15 kV, current of 20 nA, beam spot diameter of 5 μm and a 10-30 s counting time on peak. The results were calibrated against standards of natural silicates, oxides, and specpure metals, with the analytical precision for most elements estimated to be better than 1.5%. A program based on the ZAF produce was used for data correction.

Total inorganic and organic carbon analyses

Total inorganic carbon (TIC) and organic carbon (TOC) contents were analyzed at the ALS Chemex, China. Abundances of TIC were measured with an Ethanolamine Color Coulomb Instrument after being treated with $HClO_4$. The precision of the analyses (1σ) was better than 0.2%. For the TOC analyses, 200 mg rock powders were first treated with 20 vol% HCl at 50 °C for 24 h to remove carbonate, and then washed with DI water to remove residual HCl. After that, the samples were dried overnight at 50 °C and then analyzed using a LECO CS-400 analyzer. The precision of the analyses (1σ) was better than 0.1%.

Scanning electron microscopy based automated mineralogy analysis

Representative samples with relatively low (1104b with $C_{organic}$ of 0.19 wt%), intermediate (1103b with $C_{organic}$ of 0.63 wt%), and high (1104d with $C_{organic}$ of 1.10 wt%) TOC contents were further selected for scanning electron microscopy-based automated mineralogy (SEM-AM) analysis at the IGGCAS. The SEM-AM is a combined analytical method designed for the characterisation of ores and mineral processing products. Measurements began with the collection of backscattered electron (BSE) images with a ZEISS Merlin field emission scanning electron microscope (FE-SEM) on thin sections of the above samples. The spatial resolution of the FE-SEM is 0.8 nm at 15 kV. Subsequently, energy dispersive X-ray spectra (EDS) analysis was performed on each sample over an approximate 8000×900 μm area, using a Bruker QUANTAX EDS according to the BSE image adjustments. Mineral identification and analyses were automatically carried out by classification of the sample EDS spectra against a list of approved reference EDS spectra, using an equipped advanced mineral identification and characterization system software package with the particle analysis pattern.

Carbon isotope analysis

Carbon and oxygen isotope analyses of carbonate minerals were performed using the method described in Chen et al. (2005). Isotopic ratios were determined using a Finnigan MAT 253 mass spectrometer at the IGGCAS. Given that our samples contain siderite and ankerite, which normally require and extended time (e.g., 96 h at 25°C) to be fully digested with phosphoric acid relative to calcite (60 min at 72°C), an off-line method was employed instead of the continuous flow mode. Thus, it was possible to keep a vacuum condition during the whole analysis procedure. Carbon and oxygen isotope data were calibrated to the Vienna Pee Dee Belemnite (VPDB) and the standard mean ocean water (SMOW) scales, respectively. Analytical reproducibilities were better than 0.15‰ and 0.20‰ for $\delta^{13}C$ and $\delta^{18}O$, respectively, based on multiple analyses of the standards IAEA-603 ($\delta^{13}C$ = 2.46‰, $\delta^{18}O$ = −2.37‰) and IAEA-CO-8 ($\delta^{13}C$ = −5.76‰, $\delta^{18}O$ = −22.7‰). Analyses of organic matter in bulk rock powder were also conducted at the IGGCAS with a Finnigan MAT 253 mass spectrometer. Sample preparation and analytical details follow a previously devised protocol (Tong et al., 2021). The results were calibrated to the VPDB scale. Two standard materials, GBW04407 ($\delta^{13}C$ = −22.4‰) and IAEA-600 ($\delta^{13}C$ = −27.5‰), were analyzed for 5 numbers of

unknowns within each run to ensure a reproducibility of better than 0.06‰ (Table S2).

RESULTS

Mineral composition and distribution of OM in the BIF samples

The BIFs are grayish-white in color in hand sample and are finely banded with iron-rich bands ranging in thickness from 2 mm to a maximum thickness of about 1 cm. These iron-rich bands alternate with silica-rich bands of more variable thickness (Fig. 2). Generally, the contacts between these two types of bands are gradational, although minor deformation may be present locally (Fig. 3a). Given that the cummingtonite (see below), which is proposed to be metamorphic in origin in BIFs (Klein, 2005), is oriented and distributed along the lineation of the deformation, this deformation may have been formed during metamorphism. Dominant minerals in the iron-rich bands include magnetite, grunerite and siderite, as well as minor cummingtonite, ankerite, pyrite and brunsvigite (Table S1), while coarser (0.2-0.4 mm) almandine grains and/or calcite aggregates are also observed in places in some samples (Fig. 3b and Table S1), indicating a lower amphibolite facies metamorphic grade for these samples. The magnetite grain size is most commonly about 0.1 mm in diameter (Fig. 3a), although some iron-rich bands show recrystallized aggregates of up to 0.3 mm (Fig. 3b). The grunerite is subhedral to euhedral in shape (0.1-0.2 mm) (Fig. 3b), and normally intergrows with magnetite and siderite (Fig. 3a), although sometimes networks of grunerite crystals are developed alongside the magnetite and quartz interface (Fig. 3b). Similar to the grunerite, the fine-grained siderite (< 0.2 mm) occasionally occurs as independent siderite-rich networks which contain minor magnetite, grunerite and/or brunsvigite (Fig. 3a and c). By comparison, the silica-rich bands mainly consist of fine-grained quartz (0.05 to 0.1mm), although minor dusty magnetite, as well as fine-grained siderite, grunerite and pyrite (Fig. 3a and f) are also preserved in the matrix of quartz in places.

Abundant graphite is disseminated as microscopic particles (< 10 μm) in siderite (Fig. 3d), calcite (Fig. 3g) and grunerite (Fig. 3e, h, and i) grains, within both the iron- and silica-rich bands. Within single crystals of grunerite, minor magnetite particles (≤ 5 μm) were always observed within or around the grunerite grains (Fig. 3e). Moreover, a relatively high abundance of graphite also occurs outside the magnetite grains (Fig. 3e). By comparison, while graphite also occurs within the magnetite grains, it is present at a considerably lower abundance (Fig. 3j). In addition, minor

microscopic graphite grains (< 10 μm) are also found to be closely related to the widely distributed pyrite grains of variable size (10 to 30μm) in both the iron- (Fig. 3d) and silica-rich (Fig. 3f) bands.

The mineral components, distributions and weight percent based on the SEM-AM analysis of three representative BIFs samples are shown in Fig. 4. In general, sample 1104d has the highest grunerite and magnetite contents of 53.76 wt% and 27.36 wt%, respectively, with the lowest quartz content of 8.58 wt% and graphite content of 0.39 wt% among the analyzed samples. By comparison, sample 1103b has an intermediate abundance of quartz (54.35 wt%) as well as the highest siderite (14.24 wt%) and feldspar (10.32 wt%) and the lowest magnetite (2.25 wt%) contents, while sample 1104b is distinguished by the highest abundances of quartz (72.85 wt%) and graphite (3.80 wt%).

To further quantify the association of graphite with other minerals, the SEM-AM analysis results were computed by software to obtain the mineral association data (Table 1). These data describe the direct contact of graphite in relation to its associated minerals. The values are expressed as % association. Based on the results of mineral association parameters in Table 1, it can be seen that the greatest amount of graphite in these samples is associated with silicates. For example, in sample 1104d graphite has a 59.9% association with grunerite, while in sample 1104b graphite has a 50.8% association with grunerite. However, for the full sample set, mineral associations can vary, and relate to the relative abundance of each mineral. For instance, the graphite in sample 1104d exists in contact with calcite (14.6%), whereas in samples 1103b and 1104b, which have low calcite contents (1.38 wt% and 2.54 wt%, respectively), the association of graphite and calcite are insignificant (3.3% and 0.6%, respectively). Moreover, graphite in both 1103b and 1104b is also closely associated with quartz (54.2% and 28.4%, respectively).

Major element geochemistry

Results of whole-rock major element analyses are listed in Table 2. The contents of SiO_2 and Fe_2O_3 (representing total iron as Fe_2O_3) for fifteen BIF samples range from 30.2 to 82.6wt% and from 12.9 to 54.0wt%, respectively. The Al_2O_3 contents are normally low for most samples, varying from 0.19 to 1.19wt%, indicating the incorporation of a minor clastic component during deposition. By comparison, high Al_2O_3 concentrations for samples 1103b (4.42 wt%) and 1103c (3.68 wt%) suggest that a terrigenous detrital source was an important component. The contents of MgO and CaO are highly variable for all samples, ranging from 0.90 to 4.31 wt% and from 0.74 to 4.87 wt%,

respectively. The former may be related to the different silicate mineral contents in these samples, while the latter likely relates to the variable abundance of calcite (Table S1). Other oxides, such as MnO, Na_2O, K_2O and P_2O_5 are consistently low (<1.0 wt%) in all samples. In addition, variable contents of SO_3 (0.17 to 1.80 wt%) were also obtained for these samples, in line with the presence of pyrite observed microscopically.

Bulk carbon contents and isotope geochemistry

The TIC and TOC contents, as well as carbon isotope ratios, for the carbonate and organic carbon, are presented in Table 2. The studied BIF samples have a relatively large range in TIC, between 0.37 and 1.92wt%, which is comparable to other carbonate-bearing BIFs (e.g., Tong et al., 2021; 0.92 to 3.36wt%), and consistent with the highly variable LOI values (Table 2). The TOC abundances are also highly variable, ranging from 0.19 to 1.10wt% (0.55 wt% on average, n = 15), with some samples having much higher TOC contents than most Precambrian BIFs (< 0.5 wt%; Klein, 2005). Similarly, bulk rock inorganic carbon ($\delta^{13}C_{carb}$) and organic carbon ($\delta^{13}C_{organic}$) isotopic ratios for our BIF samples are variable, between -16.73 and -6.33‰ (average of -11.1‰) and between -23.81 and -15.36‰ (average of -19.94‰), respectively (n = 15). It is also noted that positive correlations exist between Fe_2O_3 and TOC (r = 0.46) and between TIC concentrations and $\delta^{13}C_{organic}$ ratios (r = -0.67), while a moderate negative correlation exists between $\delta^{18}O$ and $\delta^{13}C_{carb}$ (r = 0.64) (Fig. S2).

DISCUSSION

Source and origin of OM in BIF samples

Although there is persuasive evidence that life emerged early in Earth's history and has persisted for well over 3.5 billion years (e.g., Hofmann et al., 1999; Allwood et al., 2006; Planavsky et al., 2021), caution is required when studying early traces of life (e.g., OM, or ^{13}C-depleted graphite as the metamorphic equivalent) in Earth's rock record. Contamination of geological samples can be particularly problematic, due to both incorporation of non-indigenous compounds into the rocks after burial, and/or addition of anthropogenic organic contamination from drilling, storage, or sample preparation (e.g., Brocks et al., 2008; Rasmussen et al., 2008). For this study, ultraclean analysis (see *Sample preparation*) was conducted to ensure that all organic matter was originally part of the BIF. Moreover, direct SEM and Raman analyses on the unexposed, fresh surface of a rock

fragment from sample 1104d reveal the presence of a graphite grain (Fig. 5) that is morphologically indistinguishable from those of the polished thin sections (Fig. 3g-j). Significantly, when observed at higher resolution it is common to see the intergrowth of fine-grained graphite and apatite (Fig. 5b), which further excludes any possible organic contamination. In addition, random Raman analysis was conducted on the epoxy used to fix our samples at variable powers (0.1 to 1.0 mW), which reveals that the epoxy has significantly different spectra from graphite grains in the studied BIF (Fig. 6a). Collectively, these observations indicate that the OM was not introduced during the polishing and analysis procedures and is a primary feature of the original samples.

It is also noteworthy that the Raman spectra of graphite grains in various BIF samples yield a narrow range of crystallization temperatures (Table S3), varying from 414 to 555 °C, with the most probable temperature of ~470°C (Fig. 6b). This temperature is compatible with the greenschist to lower amphibolite metamorphic grade (450-550 °C) documented for the ca. 2.50 Ga regional metamorphism (Shen et al., 2005; Lv et al., 2012) and the lower amphibolite-facies metamorphism indicated by the mineral association (almandine + grunerite + cummingtonite) of our BIF samples. Furthermore, it has been documented that apatite in BIFs is commonly diagenetic (Dodd et al., 2019a, b) or primary (Rasmussen et al., 2021) in origin. Thus, the close association of graphite with apatite (Fig. 7a-b and d), when combined with the above measured crystallization temperatures, further implies that the observed graphitic carbon is a syngenetic and prograde phase, rather than a non-indigenous product incorporated into the samples after burial. Moreover, since Al-rich minerals in BIFs are typically detrital in origin and sourced from weathered continental rocks (Klein, 2005), the presence of chlorite (Fig. 7b) and feldspar (Fig. 7c) in close association with graphite in some samples indicates that the OM may have been partially sourced from the detritally enriched, shallow-marine environment (e.g., Dodd et al., 2019a). Nevertheless, it is also noted that there is a stronger correlation between TOC and Fe ($r = 0.46$) than for TOC and Al ($r = 0.16$) (Fig. S2), indicating that OM in the Zhalanzhangzi BIF was mainly derived from areas of ferric iron production, or was preferentially co-precipitated with ferric minerals (e.g., Lalonde et al., 2012).

The generation of ferric iron minerals in BIF depositional settings is normally ascribed to the metabolic activity of planktonic bacteria in the oceanic photic zone (e.g., Konhauser et al., 2017; Mänd et al., 2021; also see Rasmussen et al., 2014; Tosca et al., 2016 for alternative models). This means that the deposition of Precambrian BIFs would have occurred in regions of high biological

productivity, regardless of whether aqueous Fe(II) was oxidized by oxygen sourced from cyanobacteria or their predecessors (e.g., Cloud 1973), or by anoxygenic photoautotrophic Fe(II)-oxidising bacteria (i.e., photoferrotrophs, Hartman 1984; Konhauser et al., 2002). Moreover, it has been documented that most bacteria have negatively charged surfaces at neutral pH (Fein et al, 1997), while ferric (oxyhydr)oxides have a positive surface charge at the same pH (Sverjensky and Sahai, 1996). In this regard, it is reasonable to propose that some of the biomass (or OM) may have been captured by Fe(III) minerals and then preserved in BIFs, since their opposite surface charge at neutral pH favored the formation of ferric (oxyhydr)oxides (e.g., Konhauser et al., 2017; Thompson et al., 2019).

Notably, thermal disproportionation of Fe-carbonates (siderite) can also yield graphite and magnetite, and has been suggested as a possible mechanism for graphite formation in amphibolite facies rocks (Perry Jr and Ahmad, 1977; Van Zuilen et al., 2002). Even though graphite-associated siderite is found in some of our BIF samples (Fig. 3d), this is not the first-order control on the spatial distribution of graphitic carbon, as evidenced by the absence of siderite in sample 1104d (Fig. 4) and the consistently low association between siderite and graphite in samples 1103b and 1104b (9.7% and 2.5%, respectively; Table 1). Furthermore, the above process is also incompatible with the fact that there is a high siderite content (14.24 wt%) but very low abundance of graphite (0.5 wt%) in sample 1103b (Fig. 4). In addition, magnetite is a common effective catalyst in Fischer-Tropsch-type reactions, during which CO_2 and H_2 are converted into a wide spectrum of abiogenic hydrocarbons (e.g., McCollom, 2013; Nan et al., 2021). However, this process requires a H_2-rich condition that can be produced by hydrothermal alternation of ultramafic rocks (McDermott et al., 2015). The absence of ultramafic rocks (or mafic volcanics) along with the studied BIF indicates that Fischer-Tropsch-type reactions were likely insignificant. It is also noteworthy that the negative $\delta^{13}C_{organic}$ values, ranging from -23.81 to -15.36‰, for graphitic carbon in the Zhalanzhangzi BIF are consistent with biological kerogen, rather than an abiogenic origin from carbonate reduction (with a $\delta^{13}C$ signature between -12 and -10‰; Van Zuilen et al., 2002; Ohtomo et al., 2014). Meanwhile, the negative values largely overlap with isotope compositions of carbon produced by cyanobacteria and photosynthetic bacteria (-40 to -10‰) found in nature (e.g., Mojzsis et al., 1996), implying that the observed graphite grains are the metamorphic product of early biogenic organics.

Furthermore, considering that the formation of apatite [$Ca_5(PO_4)_3(F, Cl, OH)$] requires

phosphorus, which could be partially derived from the decomposition of phosphorus-bearing biomass during early diagenesis (e.g., Dodd et al., 2019b), the association of ^{13}C-depleted organic carbon and apatite is accepted as a typical feature of sediments incorporating biomass (She et al., 2014; Papineau et al., 2016). On this basis, the presence of isotopically-light graphitic carbon associated with apatite in Precambrian BIFs has been used as evidence to argue for early life in oceans (e.g., Nutman, 2007; Papineau et al., 2016; Dodd et al., 2017). As mentioned before, the intergrowth of apatite rosettes with graphite grains, which have an average $\delta^{13}C_{organic}$ value of -19.94‰ (Table 2), is observed in our samples (Fig. 5b). This supports a biological origin for the graphite. In addition, the presence of graphite inclusions in apatite in our samples (Fig. 7d and Fig. S3) is consistent with those observed in Neoarchean to Paleoproterozoic BIFs subjected to low-grade metamorphism (Dodd et al., 2019b), implying this phenomenon is unrelated to metamorphic grade. Thus, consistent with previous studies (e.g., Dodd et al., 2019b), the apatite with graphite inclusions likely represents the remineralization of biogenic organics.

Nevertheless, a fluid-depositional pathway, rather than a biological origin, for graphite associated with apatite in metamorphosed BIF has also been proposed (e.g., Lepland et al., 2011; Papineau et al., 2011). Moreover, Dodd et al (2019b) highlighted the widespread occurrence of two types of graphite (i.e., crystalline graphite representing the metamorphosed product of syngenetic organic carbon deposited in BIF, and poorly crystalline graphite precipitated from fluids sourced from syngenetic carbon), through a detailed examination of ten variably metamorphosed BIFs ranging in ages from >3.8 to 1.8 Ga. As shown in Fig. 6b, all the studied graphite grains in our samples have a consistent crystallization temperature (~470℃, see Table S3) that matches that predicted for the regional metamorphic grade (450-550 ℃). In addition, retrograde minerals such as greenalite and minnesotaite that replace grunerite, and secondary veins containing poorly crystalline carbon of fluid-depositional origin (e.g., Dodd et al., 2019b), are absent from our samples. Taken together, the ^{13}C-depleted graphite in the Zhalanzhangzi BIF is likely biological in origin, representing the remineralization and metamorphism of syngenetic biomass.

Carbon isotope evidence for OM oxidation during BIF formation

It is generally agreed that the observed minerals in BIFs are not primary in origin but reflect the products of multiple post-depositional alteration processes that occurred under both diagenetic and

metamorphic conditions (e.g., Bekker et al., 2014; Konhauser et al., 2017). The initial water column precipitate of BIF has been proposed to be ferric (oxyhydr)oxides formed in the photic zone (Holland, 1973; Morris, 1993) or to be green rust, a ferrous-ferric hydroxy salt, generated when there was abundant Fe(II) (e.g., Zegeye et al., 2012; Halevy et al., 2017). The ferric (oxyhydr)oxides would subsequently transform to Fe(III)-Si gel during deposition (Percak-Dennett et al., 2011) in the presence of high dissolved silica (~2.2 mM) in Precambrian seawater (Jones et al., 2015), and would be preserved as magnetite or iron carbonates in sediments when the remineralization of buried OM was coupled to Fe(III) reduction (Konhauser et al., 2005; Johnson et al., 2008; Mänd et al., 2021). Alternatively, green rust would age directly to magnetite within the water column and sediments (Halevy et al., 2017; Li et al., 2017). It is important to note that although greenalite has also been suggested as a primary precipitate that formed in the water column (Rasmussen et al., 2015, 2016, 2017), the large iron isotope ratios documented for Archean BIFs (e.g., Johnson et al., 2008) are inconsistent with small iron isotopic effects induced by direct seawater precipitation of greenalite (Mänd et al., 2021).

Estimates of the initial amount of OM precipitated in BIFs based on C isotope and magnetite mass balance suggests relatively high TOC contents of ~4.7 wt% in Precambrian BIFs. These concentrations are comparable with those measured in coeval black shales (e.g., Konhauser et al., 2017), supporting the interpretation that large amounts of OM may have been respired via microbial dissimilatory iron reduction (DIR) during diagenesis or thermal decomposition during metamorphism. Calculations of the minimum total primary OM content (see Tong et al., 2021 for the calculation method) precipitated in the Zhalanzhangzi BIF (0.74 to 1.82 wt%, 1.15 wt% on average; Table S4) support the above suggestion that part of the OM may have been respired via DIR. Significantly, although this value is lower than the estimation by Konhauser et al. (2017), it is much higher than the actual measured TOC content of our samples (average of 0.55 wt%), and indicates that more than 50% of the primary OM has likely been consumed (Table S4).

Nevertheless, the generally extremely low TOC contents (<0.1 wt%, e.g., Beukes et al., 1990; Beukes and Klein, 1990; Kaufman, 1996; Klein, 2005), when combined with the absence of OM (or graphite) in clays within some Precambrian BIFs (Dodd et al., 2019a), has been argued as evidence for minimal OM production during BIF deposition. Despite the relatively high TOC content measured in the Zhalanzhangzi BIF, the carbonate phases (i.e., siderite, ankerite and calcite) in this

BIF also have highly negative $\delta^{13}C_{carb}$ values (-11.1‰ on average, n = 15). Given that carbon isotope fractionation between calcite and siderite at near-equilibrium with the water mass is about -0.5‰ (at 25 °C; Jiménez-López et al., 2001; Jiménez-López and Romanek, 2004), estimated $\delta^{13}C$ values for siderite formed in equilibrium with Archean seawater with $\delta^{13}C$ value of ~0‰ should range from -1.5 to -0.5‰ (Tong et al., 2021). In this regard, the highly negative $\delta^{13}C_{carb}$ values, ranging from -16.73 to -6.33‰, in the Zhalanzhangzi BIF are unlikely to be of seawater origin. This is the case even if the water column which precipitated the BIF was overprinted by hydrothermal fluids bearing mantle-derived dissolved inorganic carbon with a $\delta^{13}C$ value around -6.5‰ (Shanks III, 2001). Moreover, the relatively uniform $\delta^{13}C$ values of iron-poor carbonates deposited synchronously in the late Archean, across a wide range of water column depths from continental shelf to deep basin, argues against vertical stratification with respect to carbon isotopes in dissolved inorganic carbon (DIC) at that time (Fischer et al., 2009). This further precludes the possibility that the negative $\delta^{13}C_{carb}$ values in the Zhalanzhangzi BIF are related to direct carbonate precipitation from seawater that was stratified with respect to $\delta^{13}C$.

Isotopically light $\delta^{13}C$ in carbonate minerals may also implicate metamorphism, which can be parsed when paired with oxygen isotopes (e.g., Kaufman et al., 1990; Carrigan and Cameron, 1991; Li et al., 2013), as carbonates from metamorphosed BIFs typically have extremely low $\delta^{18}O$ (Yang et al., 2015). However, such alteration would produce lighter $\delta^{18}O$ without altering $\delta^{13}C_{carb}$, assuming a rock-buffered diagenetic environment comparable to that of BIFs (Jaffrés et al., 2007; Knauth and Kennedy, 2009). Despite this, hydrothermal alteration has been suggested to have influenced $\delta^{13}C$ values in carbonates, producing negative $\delta^{13}C$ and positive $\delta^{18}O$ (Shanks III et al., 1995). At first glance, the moderate negative correlation between $\delta^{13}C_{carb}$ and $\delta^{18}O$ values for our samples (Fig. S2) may appear compatible with the above situation, but we preclude this interpretation due to the absence of petrographic evidence (e.g., alterations and veinlets) and geochemical characteristics (e.g., variations in bulk rock trace element composition, not shown) that normally accompany hydrothermal alteration.

In addition, it has been proposed that because manganese oxides are significantly enriched in ^{18}O compared to seawater (e.g., Mandernack et al., 1995), there would be a negative correlation between $\delta^{13}C_{carb}$ and $\delta^{18}O$ values during diagenetic Mn oxide reduction and subsequent Mn carbonate precipitation (e.g., Neumann et al., 2002; Dong et al., 2022). Considering that Fe has

similar chemical properties to Mn (Armstrong, 2008), we suggest that in agreement with current models for BIF formation (e.g., Beukes and Gutzmer, 2008), the observed negative correlation between $\delta^{13}C_{carb}$ and $\delta^{18}O$ values in our BIF samples may also have been formed during diagenetic Fe(III) reduction. This conclusion is supported by our SEM and Raman analyses, which reveal the reduction of Fe(III) minerals by OM during diagenesis or metamorphism (see the following sections). Furthermore, variations in $\delta^{13}C_{carb}$ values for the carbonates are likely related to the relative contributions of different carbon sources during the diagenetic formation of carbonates. However, considering the positive correlation between $\delta^{13}C_{carb}$ values and TIC contents (r = 0.67; Fig. S2), seawater DIC appears to have been the dominant carbon source for the carbonate minerals.

The fate of OM in iron- and silica-rich BIF bands

Detailed observations on the Zhalanzhangzi BIF samples indicate that OM (i.e., graphite) tends to be unevenly distributed in the iron- and silica-rich bands (Fig. 8a). In iron-rich bands, abundant fine-grained graphite grains (< 10μm) are always closely associated with magnetite, siderite, pyrite and calcite (Fig. 8b). Significantly, if we accept that ferric (oxyhydr)oxides were the primary mineral forming the Zhalanzhangzi BIF, then formation of the magnetite, siderite and pyrite would need Fe(II) that could have been (or at least partially) sourced from DIR (e.g., Klein, 2005; Johnson et al., 2008; Li et al., 2013). At higher resolution, it is common to observe the presence of fine-grained (< 10 μm) magnetite (Fig. 8c), siderite (Fig. 8d) and pyrite (Fig. 8e) preserved within or in close association with graphite grains. Notably, all graphite grains in the above cases have consistent crystallization temperatures (Fig. 6b) that are comparable to the prograde crystallization temperature of the Zhalanzhangzi BIF, indicating that they should be relicts of primary OM that has been subjected to oxidation and metamorphism. In addition, carbonate minerals, such as siderite, ankerite and calcite, which are documented to be by-products of the DIR process (e.g., Konhauser et al., 2005, 2017), are widely distributed in the iron-rich bands (Fig. 4), and are closely associated with graphite (Fig. 8d-e). The above associations are readily explained by reactions between ferric (oxyhydr)oxides and OM, during which the Fe(II) produced is expected to react with additional ferric (oxyhydr)oxides to form magnetite, or with HCO_3^- and S^{2-} (or HS^-) to generate siderite and pyrite, respectively, within the sediment porewater. Among all ^{13}C-depleted carbonate minerals ($\delta^{13}C_{carb}$ = -11.1‰ on average, n = 15), siderite in this BIF is likely to be an early product formed within the sediment porewater,

whereas ankerite and calcite likely represent diagenetic and metamorphic alteration of early siderite, respectively (e.g., Klein, 2005; Pecoits et al., 2009). The suggestion that the origin of calcite is from prograde metamorphism is supported by the replacement of siderite by coarse-grained calcite and the existence of siderite relict edges in coarser calcite grains (Fig. 8f). It is also noteworthy that although OM in iron-rich bands of the Zhalanzhangzi BIF show typical features of oxidation coupled to ferric iron reduction, the slightly positive correlation between TOC and Fe (r = 0.46, Fig. S2), in combination with the close associations of OM with iron-bearing phases, indicates that ferric (oxyhydr)oxides likely exerted a first order control on the abundance of OM.

By comparison, graphite is a minor component in the silica-rich bands (Fig. 8a), although in places a considerable amount of graphite was observed alongside the siderite and chlorite rims (Fig. 8g). Normally, the graphite exhibits anhedral to sub-spherical morphologies, and is sealed in quartz grains (Fig. 8g). This is in contrast to those observed in the iron-rich bands, where graphite always shows mineralogical signs of oxidation coupled to ferric iron reduction (e.g., the presence of graphite in association with Fe(II)-bearing minerals and/or carbonates). Nonetheless, the existence of graphite grains in silica-rich bands may indicate that the amorphous silica, which deposited during intervals of iron deposition (Posth et al., 2008) or was coprecipitated with primary ferric (oxyhydr)oxides (Ewers, 1983; Fischer and Knoll, 2009), was also able to capture and preserve OM. The primary amorphous silica is inferred to transform to quartz (e.g., Trendall, 1983; Klein, 2005) during the lower amphibolite-facies metamorphism identified for the Zhalanzhangzi BIF. Given that silicate minerals have the ability to protect OM from bacterial degradation (e.g., Keil et al., 1994; McMahon et al., 2016), OM bound to amorphous silica is thus expected to persist through recrystallisation. This assumption is in line with the observation that graphite in our BIF samples is closely associated with quartz grains, among which the SEM-AM analysis reveals an association up to 54.2% for these minerals in sample 1103b (Table 1). In addition, in contrast to previous studies that argued there is generally an absence of OM bounded to silicate minerals in Precambrian BIFs (Dodd et al., 2019a), we identify the existence of graphite within grunerite grains in our samples (Fig. 3h and 7c). The SEM-AM analyses (Table 1) on samples 1104b and 1104d also show relatively high associations for graphite with grunerite (59.9%) and for graphite with chlorite (50.8%), indicating that silicate minerals in BIF can also capture and preserve OM (e.g., Haugaard et al., 2017), irrespective of whether the silicates were primary water column precipitates (e.g., Rasmussen et al., 2017) or

formed during late-diagenesis (Klein, 2005). These observations, when combined with the close association of graphite with quartz discussed above, may help to explain why more than 40% of OM in the Zhalanzhangzi BIF (Table S4) was devoid of oxidation and subsequently transferred to graphite during the greenschist to lower amphibolite facies regional metamorphism (Shen et al., 2005; Lv et al., 2012).

Implications for BIF-dependent Archean carbon cycling

Carbon is an element that undergoes important biogeochemical oxidation-reduction reactions at the Earth's surface (Berner, 1989), among which mineralization of OM can result in accumulation of greenhouse gasses like methane, while its burial can be a net source of oxidants (e.g., oxygen) and a net sink of CO_2 (Berner, 2003; Crowe et al., 2008; Keil, 2011). Therefore, biogeochemical cycles of carbon over geological time exert major long-term controls on atmospheric chemistry (Berner, 2003; Lalonde et al., 2012; Friese et al., 2021). Nevertheless, carbon cycles in modern and Archean marine sediments may have been different, depending on the species of oxidants presented. In oxygenated and sulfate-rich modern marine sediments, OM is mainly consumed by aerobic respiration and sulfate reduction (e.g., Jørgensen, 1982; Froelich et al., 1979). By comparison, in the absence of oxidants such as oxygen, sulfate and nitrate in Archean marine sediments (Strauss, 2003; Anbar et al., 2007; Godfrey and Falkowski, 2009), the carbon cycle is expected to have been more closely coupled to Fe cycling, in BIFs in particular, because the ferric minerals in BIFs would have been the most accessible electron acceptor for OM oxidation (e.g., Walker, 1987; Nealson and Myers, 1990; Konhauser et al., 2005).

The very low $\delta^{13}C_{carb}$ values for carbonate minerals (Table 2) and the presence of OM-bearing apatite associated with magnetite (Fig. S3) in our BIF samples all point to OM oxidation by Fe(III), supporting the assumption that carbon cycling linked to Fe would have been an important process in Archean BIFs. However, if BIFs were deposited from an OM-starved water column (Dodd et al., 2019a), the significance of BIF-dependent carbon cycling would have been negligible. As discussed above, ferric (oxyhydr)oxides likely controlled the abundance of OM in the Zhalanzhangzi BIF. This is similar to the situation for the Transvaal BIF, which also shows a positive correlation between TOC and Fe ($r = 0.74$; Klein and Beukes, 1989). In this respect, if we accept the "upwelling model", in which dissolved Fe(II) is biologically oxidized in the photic zone to form the ferric

(oxyhydr)oxides (e.g., Bekker et al., 2014; Konhauser et al., 2017; Tong et al., 2021), the above observations indicate that the deposition of Precambrian BIFs largely occurred in regions of high biological productivity. This conclusion is supported by the "upside-down" biosphere proposed for the Archean Eon (Walker, 1987), during which regions of high biological productivity would have been underlain by Fe(III)-rich sediments produced by photosynthesis (Cloud, 1973).

Low OM contents in BIFs have also been attributed to the physical properties of iron oxides and the high silica concentrations of Archean seawater. For the first point, because oxidized iron is denser than cell material and organic compounds, it would have settled more rapidly than particulate OM, producing sediments rich in oxidized iron and deficient in OM (Walker, 1987). However, the opposite surface charges for bacterial cells and ferric (oxyhydr)oxides (Sverjensky and Sahai, 1996; Fein et al, 1997) would lead to a strong attraction between these two components, manifest as encrustation of bacterial cells and formation of cell and ferric (oxyhydr)oxide aggregates (Konhauser, 1998; Kappler and Newman, 2004). For the second point, although some laboratory experiments with photosynthetic bacteria have revealed that the photoferrotroph cell surfaces would repel iron (oxyhydr)oxides in the presence of silica (Thompson et al., 2019), observations on Chocolate Pots hot springs indicated that even at silica concentrations higher than that estimated for the Precambrian oceans, ~80% of the silica-rich hydrous ferric oxides would co-precipitate with, and be reduced by, the microbial communities (e.g., Percak-Dennett et al., 2011; Fortney et al., 2016). Moreover, high silica contents have been documented to be able to hinder the transformation of poorly crystalline ferric (oxyhydr)oxides into more crystalline minerals (Friese et al., 2021), and therefore would have facilitated the reaction between OM and iron (oxyhydr)oxides in Precambrian oceans. It is also noted that the OM co-precipitated with iron, as estimated by Trendall (2002), is comparable to the ratio of ferrihydrite to carbon substrate left at the end of DIR incubations in culturing experiments (Roh et al., 2003; Roden, 2003). Thus, we suggest that labile OM would have been co-precipitated with ferric (oxyhydr)oxides in Archean oceans and was subsequently oxidized by Fe(III), in the absence of other oxidants, to produce Fe(II) in the sediments.

Collectively, photosynthesis in Archean oceans would have led to the fixation of CO_2 and the production of precursor ferric (oxyhydr)oxides in BIFs (e.g., Konhauser et al., 2017). Following its generation, the ferric (oxyhydr)oxide would have adsorbed OM produced by photosynthesis, and this OM was significantly consumed to form the Fe(II)-bearing phases in BIFs. Significantly, the

remineralization of OM coupled to iron reduction would release phosphorus and other nutrients from both the biomass and from the ferric (oxyhydr)oxides (e.g., Ingall et al., 1993; Ruttenberg and Berner, 1993; Van Cappellen and Ingall, 1994; Bjerrum and Canfield, 2002). Although a proportion of the P released to pore waters may subsequently switch to authigenic phases such as carbonate fluorapatite (Ruttenberg and Berner, 1993) or vivianite (e.g., Dijkstra et al., 2014; Xiong et al., 2019), as well as being reabsorbed to ferric (oxyhydr)oxides at the sediment-water interface (e.g., Slomp and Van Raaphorst, 1993; Slomp et al., 1996), some of the P released may have been recycled back to the water column (Alcott et al., 2022). Given that the Archean biosphere is thought to have been predominantly P-limited (e.g., Kipp and Stüeken, 2017; Reinhard et al., 2017; Guilbaud et al., 2020), this BIF-dependent carbon cycling may have been an important source of P and other nutrients to the water column, helping to sustain a degree of productivity.

Acknowledgements and Funding

The authors are grateful for the assistance of associate Prof. Ying-xia Xu, Dr. Xiao-xue Tong and Bang-lu Zhang during field work. The authors also appreciate the use of Raman spectroscopy, scanning electron microscopy and energy dispersive spectroscopy from the Institute of Deep-sea Science and Engineering, Chinese Academy of Sciences, Sanya, China. We thank Editor Don R. Baker and Jie Xue for handling the manuscript, and two anonymous reviewers for their insightful comments. This work was financially supported by the National Natural Science Foundation of China (No. 42272082, 42150104, 42106069 and 42006061), the Key Research Program of the Institute of Geology and Geophysics, Chinese Academy of Sciences (grant IGGCAS-201905 and IGGCAS-202204) and the Youth Innovation Promotion Association and Key Research Program of Frontier Sciences (grant ZDBS-LY-DQC037) of the Chinese Academy of Sciences.

References cited

Allwood, A.C., Walter, M.R., Kamber, B.S., Marshall, C.P., and Burch, I.W. (2006) Stromatolite reef from the Early Archaean era of Australia. Nature, 441, 714–718.

Anbar, A.D., Duan, Y., Lyons, T.W., Arnold, G.L., Kendall, B., Creaser, R.A., Kaufman A.J., Gordon, G.W., Scott, C., Garvin, J., and Buick, R. (2007) A Whiff of Oxygen Before the Great Oxidation

Event? Science, 317(5846), 1903–1906.

Armstrong, F.A. (2008) Why did nature choose manganese to make oxygen? Philosophical Transactions of the Royal Society B, Biological Sciences, 363(1494), 1263–1270.

Alcott, L.J., Mills, B.J.W., Bekker, A., and Poulton, S.W. (2022) Earth's Great Oxidation Event facilitated by the rise of sedimentary phosphorus recycling. Nature Geoscience, 15, 210–215.

Berner, R.A. (1989) Biogeochemical cycles of carbon and sulfur and their effect on atmospheric oxygen over Phanerozoic time. Global and Planetary Change, 1(1–2), 97–122.

Beukes, N.J., Klein, C., Kaufman, A.J., and Hayes, J.M. (1990) Carbonate petrography, kerogen distribution, and carbon and oxygen isotope variations in an early Proterozoic transition from limestone to iron-formation deposition, Transvaal Supergroup, South Africa. Economic Geology, 85(4), 663–690.

Beukes, N.J., and Klein, C. (1990) Geochemistry and sedimentology of a facies transition—from microbanded to granular iron-formation—in the early Proterozoic Transvaal Supergroup, South Africa. Precambrian Research, 47(1–2), 99–139.

Bjerrum, C.J., and Canfield, D.E. (2002) Ocean productivity before about 1.9 Ga ago limited by phosphorus adsorption onto iron oxides. Nature 417(6885), 159–162.

Berner, R.A. (2003) The long-term carbon cycle, fossil fuels and atmospheric composition. Nature, 426(6964), 323–326.

Brocks, J.J., Grosjean E., and Logan G.A. (2008) Assessing biomarker syngeneity using branched alkanes with quaternary carbon (BAQCs) and other plastic contaminants. Geochimica et Cosmochimica Acta, 72(3), 871–888.

Bekker, A., Planavsky, N., Krapež, B., Rasmussen, B., Hofmann, A., Slack, J.F., Rouxel, O.J., and Konhauser, K.O. (2014) Iron formations: Their origins and implications for ancient seawater chemistry, in Holland, H.D., and Turekian, K.K., ed., Treatise of Geochemistry: second ed. v. 9. Elsevier, p. 561–628.

Cloud, P. (1973) Paleoecological significance of the banded iron-formation. Economic Geology, 68(7), 1135–1143.

Carrigan, W.J., and Cameron, E.M. (1991) Petrological and stable isotope studies of carbonate and sulfide minerals from the Gunflint Formation, Ontario: evidence for the origin of early Proterozoic iron-formation[J]. Precambrian Research, 52(3–4), 347–380.

Chen, D., Qing, H., and Li, R. (2005) The Late Devonian Frasnian–Famennian (F/F) biotic crisis: insights from $\delta^{13}C_{carb}$, $\delta^{13}C_{org}$ and $^{87}Sr/^{86}Sr$ isotopic systematics. Earth and Planetary Science Letters, 235(1–2), 151–166.

Crowe, S.A., Jones C.A., Katsev S., Magen, C., O'Neill, A.H., Sturm, A., Canfield, D.E., Haffner, G.D., Mucci, A., Sundby, B., and Fowle, D.A. (2008) Photoferrotrophs thrive in an Archean Ocean analogue. Proceedings of the National Academy of Sciences, 105(41), 15938–15943.

Craddock, P.R., and Dauphas, N. (2011) Iron and carbon isotope evidence for microbial iron respiration throughout the Archean. Earth and Planetary Science Letters, 303(1–2), 121–132.

Czaja, A.D., Johnson, C.M., Beard, B.L., Roden, E.E., Li, W.Q., and Moorbath, S. (2013) Biological Fe oxidation controlled deposition of banded iron formation in the ca. 3770 Ma Isua Supracrustal Belt (West Greenland). Earth and Planetary Science Letters, 363, 192–203.

Chen, J., Li, H.M., Luo, D.K., Li, L.X., Yang, X.Q., Liu, M.J., Yao, T., and Hu, B. (2015) Formation age, geochemical characteristics and geological significance of the Zhalanzhangzi BIF in eastern Hebei Province. Geological Bulletin of China, 34(5), 919–929.

Dijkstra, N., Kraal, P., Kuypers, M.M.M., Schnetger, B., and Slomp, C.P. (2014) Are iron-phosphate minerals a sink for phosphorus in anoxic Black Sea sediments? PLOS ONE, 9(7), e101139.

Dodd, M.S., Papineau, D., Grenne, T., Slack, J.F., Rittner, M., Pirajno, F., O'Neil, J., and Little, C.T.S. (2017) Evidence for early life in Earth's oldest hydrothermal vent precipitates. Nature, 543(7643), 60–64.

Dodd, M.S., Papineau, D., Pirajno, F., Wan, Y.S., and Karhu, J.A. (2019a) Minimal biomass deposition in banded iron formations inferred from organic matter and clay relationships. Nature communications, 10(1), 1–13.

Dodd, M.S., Papineau, D., She, Z.B., Manikyamba, C., Wan, Y.S., O'Neil, J., Karhu, J.A., Rizo, H., and Pirajno, F. (2019b) Widespread occurrences of variably crystalline 13C-depleted graphitic carbon in banded iron formations. Earth and Planetary Science Letters, 512, 163–174.

Dong, Z.G., Peng, Z.D., Wang, C.L., Zhang, B.L., Zhang, L.C., Li, J., Zhang, X., and Zhang, L. (2022) Insight into the genesis of the Zhaosu Carboniferous Mn carbonate deposit (NW China): constraints from petrography, geochemistry, and C–Mo isotopes. Mineralium Deposita, 57, 1269–1289.

Ewers, W.E. (1983) Chemical factors in the deposition and diagenesis of banded iron-formation.

Developments in Precambrian Geology, Elsevier, 6, 491–512.

Froelich, P.N., Klinkhammer, G.P., Bender, M.L., Luedtke, N.A., Heath, G.R., Cullen, D., Dauphin, P., Hammond, D., Hartman, B., and Maynard, V. (1979) Early oxidation of organic matter in pelagic sediments of the eastern equatorial Atlantic: suboxic diagenesis. Geochimica et Cosmochimica Acta, 43(7), 1075–1090.

Fein, J.B., Daughney, C.J., Yee, N., and Davis, T.A. (1997) A chemical equilibrium model for metal adsorption onto bacterial surfaces. Geochimica et Cosmochimica Acta, 61(16), 3319–3328.

Fischer, W.W., Schroeder, S., Lacassie, J.P., Beukes, N.J., Goldberg, T., Strauss, H., Horstmann, U.E., Schrag, D.P., and Knoll, A.H. (2009) Isotopic constraints on the Late Archean carbon cycle from the Transvaal Supergroup along the western margin of the Kaapvaal Craton, South Africa. Precambrian Research, 169(1–4), 15–27.

Fischer, W.W., and Knoll, A.H. (2009) An iron shuttle for deepwater silica in Late Archean and early Paleoproterozoic iron formation. Geological Society of America Bulletin, 121(1–2), 222–235.

Fortney, N.W., He, S., Converse, B.J., Johnson, C.M., Boyd, E.S., and Roden, E.E. (2016) Microbial F e (III) oxide reduction potential in Chocolate Pots hot spring, Yellowstone National P ark. Geobiology, 14(3), 255–275.

Friese, A., Bauer, K., Glombitza, C., Ordoñez, L., Ariztegui, D., Heuer, V.B., Vuillemin, A., Henny, C., Nomosatryo, S., Simister, R., Wagner, D., Bijaksana, S., Vogel, H., Melles, M., Russell, J.M., Crowe, S.A., and Kallmeyer, J. (2021) Organic matter mineralization in modern and ancient ferruginous sediments. Nature communications, 12(1), 1–9.

Gole, M.J., and Klein, C. (1981) Banded iron-formations through much of Precambrian time[J]. The Journal of Geology, 89(2), 169–183.

Geng, Y.S. (1998) Archean Granite Pluton Events of the Qian'an Area, East Hebei Province and its Evolution. In: Cheng, Y.Q. (Eds.), Corpus on Early Precambrian Research of the North China Craton. Geological Publishing House, Beijing, pp. 92–104 (in Chinese).

Geng, Y.S., Liu, F.L., and Yang, C.H. (2006) Magmatic event at the end of the Archean in Eastern Hebei Province and its geological implication. Acta Geologica Sinica-English Edition. 80(6), 819–833 (English version).

Godfrey, L.V., and Falkowski, P.G. (2009) The cycling and redox state of nitrogen in the Archaean ocean. Nature Geoscience, 2(10), 725–729.

Guo, R.R., Liu, S.W., Santosh, M., Li, Q.G., Bai, X., and Wang, W. (2013) Geochemistry, zircon U–Pb geochronology and Lu–Hf isotopes of metavolcanics from eastern Hebei reveal Neoarchean subduction tectonics in the North China Craton. Gondwana Research, 24(2), 664–686.

Guilbaud, R., Poulton, S.W., Thompson, J., Husband, K.F., Zhu, M.Y., Zhou, Y., Shields, G.A., and Lenton, T.M. (2020) Phosphorus-limited conditions in the early Neoproterozoic ocean maintained low levels of atmospheric oxygen. Nature Geoscience, 13(4), 296–301.

Holland, H.D. (1973) The oceans; a possible source of iron in iron-formations. Economic Geology, 68(7), 1169–1172.

Hartman, H. (1984) The evolution of photosynthesis and microbial mats: a speculation on the banded iron formations. In: Cohen, Y., Castenholz, R.W., and Halvorson, H.O. (Eds.), Microbial Mats: Stromatolites. Alan R. Liss, New York, pp. 449–453.

Hofmann, H.J., Grey, K., Hickman, A.H., and Thorpe, R.I. (1999) Origin of 3.45 Ga coniform stromatolites in Warrawoona group, Western Australia. Geological Society of America Bulletin, 111(8), 1256–1262.

Heimann, A., Johnson, C.M., Beard, B.L., Valley, J.W., Roden, E.E., Spicuzza, M.J., and Beukes, N.J. (2010) Fe, C, and O isotope compositions of banded iron formation carbonates demonstrate a major role for dissimilatory iron reduction in ~2.5 Ga marine environments. Earth and Planetary Science Letters, 294(1–2), 8–18.

Halevy, I., Alesker, M., Schuster, E.M., Popovitz-Biro, R., and Feldman, Y. (2017) A key role for green rust in the Precambrian oceans and the genesis of iron formations. Nature Geoscience, 10(2), 135–139.

Haugaard, R., Ootes, L., and Konhauser, K.O. (2017) Neoarchaean banded iron formation within a~ 2620 Ma turbidite-dominated deep-water basin, Slave craton, NW Canada. Precambrian Research, 292, 130–151.

Ingall, E.D., Bustin, R.M., and Van Cappellen, P. (1993) Influence of water column anoxia on the burial and preservation of carbon and phosphorus in marine shales. Geochimica et Cosmochimica Acta, 57(2), 303–316.

Jørgensen, B.B. (1982) Mineralization of organic matter in the sea bed—the role of sulphate reduction. Nature, 296(5858), 643–645.

Jiménez-López, C., Caballero, E., Huertas, F.J., and Romanek, C.S. (2001) Chemical, mineralogical

and isotope behavior, and phase transformation during the precipitation of calcium carbonate minerals from intermediate ionic solution at 25 °C. Geochimica et Cosmochimica Acta, 65(19), 3219–3231.

Jiménez-López, C., and Romanek C.S. (2004) Precipitation kinetics and carbon isotope partitioning of inorganic siderite at 25 °C and 1 atm. Geochimica et Cosmochimica Acta, 68(3), 557–571.

Jaffrés, J.B.D., Shields, G.A., and Wallmann, K. (2007) The oxygen isotope evolution of seawater: A critical review of a long-standing controversy and an improved geological water cycle model for the past 3.4 billion years. Earth-Science Reviews, 83(1–2), 83–122.

Johnson, C.M., Beard, B.L., Klein, C., Beukes, N.J., and Roden, E.E. (2008) Iron isotopes constrain biologic and abiologic processes in banded iron formation genesis. Geochimica et Cosmochimica Acta, 72(1), 151–169.

Jones, C., Nomosatryo, S., Crowe, S.A., Bjerrum, C.J., and Canfield D.E. (2015) Iron oxides, divalent cations, silica, and the early earth phosphorus crisis. Geology, 43(2), 135–138.

Klein, C., and Beukes, N.J. (1989) Geochemistry and sedimentology of a facies transition from limestone to iron-formation deposition in the early Proterozoic Transvaal Supergroup, South Africa. Economic Geology, 84(7), 1733–1774.

Kaufman, A.J., Hayes, J.M., and Klein, C. (1990) Primary and diagenetic controls of isotopic compositions of iron-formation carbonates. Geochimica et Cosmochimica Acta, 54(12), 3461–3473.

Keil, R.G., Montluçon, D.B., Prahl F.G., and Hedges, J.I. (1994) Sorptive preservation of labile organic matter in marine sediments. Nature, 370(6490), 549–552.

Kaufman, A.J. (1996) Geochemical and mineralogic effects of contact metamorphism on banded iron-formation: an example from the Transvaal Basin, South Africa. Precambrian Research, 79(1–2), 171–194.

Konhauser, K.O. (1998) Diversity of bacterial iron mineralization. Earth-Science Reviews, 43(3–4), 91–121.

Kröner, A., Cui, W.Y., Wang, S.Q., Wang, C.Q., and Nemchin, A.A. (1998) Single zircon ages from high-grade rocks of the Jianping Complex, Liaoning Province, NE China. Journal of Asian Earth Sciences, 16(5–6), 519–532.

Konhauser, K.O., Hamade, T., Raiswell, R., Morris, R., Ferris, F., Southam, G., and Canfield, D.

(2002) Could bacteria have formed the Precambrian banded iron formations? Geology 30(12), 1079–1082.

Kappler, A., and Newman, D.K. (2004) Formation of Fe (III)-minerals by Fe (II)-oxidizing photoautotrophic bacteria. Geochimica et Cosmochimica Acta, 68(6), 1217–1226.

Klein, C. (2005) Some Precambrian banded iron-formations (BIFs) from around the world: Their age, geologic setting, mineralogy, metamorphism, geochemistry, and origins. American Mineralogist, 90(10), 1473–1499.

Konhauser, K.O., Newman, D.K., and Kappler, A. (2005) The potential significance of microbial Fe(III) reduction during deposition of Precambrian banded iron formations. Geobiology, 3, 167–177.

Konhauser, K.O., Amskold, L., Lalonde, S.V., Posth, N.R., Kappler, A., and Anbar, A. (2007) Decoupling photochemical Fe(II) oxidation from shallow-water BIF deposition. Earth and Planetary Science Letters, 258(1–2), 87–100.

Knauth, L.P., and Kennedy, M.J. (2009) The late Precambrian greening of the Earth. Nature, 460(7256), 728–732.

Keil, R.G. (2011) Terrestrial influences on carbon burial at sea. Proceedings of the National Academy of Sciences, 108(24), 9729–9730.

Konhauser, K., Lalonde, S., Planavsky, N., Pecoits, E., Lyons, T., Mojzsis, S., Rouxel, O., Fralick, P., Barley, M., Kump, L., and Bekker, A. (2011) Aerobic bacterial pyrite oxidation and acid rock drainage during the Great Oxidation Event. Nature, 478, 369–373.

Kennedy, M.J., Löhr, S.C., Fraser, S.A., and Baruch, E.T. (2014) Direct evidence for organic carbon preservation as clay-organic nanocomposites in a Devonian black shale; from deposition to diagenesis. Earth and Planetary Science Letters, 388, 59–70.

Kipp, M.A., and Stüeken, E.E. (2017) Biomass recycling and Earth's early phosphorus cycle. Science Advances, 3(11), eaao4795.

Konhauser, K.O., Planavsky, N.J., Hardisty, D.S., Robbins, L.J., Warchola, T.J., Haugaard, R., Lalonde, S.V., Partin, C.A., Oonk, P.B.H., Tsikos, H., Lyons, T.W., Bekker, A., and Johnson, C.M. (2017) Iron formations: A global record of Neoarchean to Paleoproterozoic environmental history, Earth-Science Reviews, 172, 140–177.

Liu, D.Y., Nutman, A.P., Compston, W., Wu, J.S., and Shen, Q.H. (1992) Remnants of ≥3800 Ma

crust in the Chinese part of the Sino-Korean craton. Geology, 20(4), 339–342.

Lepland, A., Van Zuilen, M.A., and Philippot, P. (2011) Fluid-deposited graphite and its geobiological implications in early Archean gneiss from Akilia, Greenland. Geobiology, 9, 2–9.

Lalonde, K., Mucci, A., Ouellet, A., and Gélinas, Y. (2012) Preservation of organic matter in sediments promoted by iron. Nature, 483, 198–200.

Lv, B, Zhai, M.G., Li, T.S., and Peng, P. (2012) Zircon U–Pb ages and geochemistry of the Qinglong volcano-sedimentary rock series in Eastern Hebei: implication for ~2500 Ma intra-continental rifting in the North China Craton. Precambrian Research, 208–211, 145–160.

Li, W.Q., Huberty, J.M., Beard, B.L., Kita, N.T., Valley, J.W., and Johnson, C.M. (2013) Contrasting behavior of oxygen and iron isotopes in banded iron formations revealed by in situ isotopic analysis. Earth and Planetary Science Letters, 384, 132–143.

Liu, C.H., Zhao, G.C., Liu, F.L., and Shi, J.R. (2014) Zircon U-Pb and Lu-Hf isotopic and whole-rock geochemical constraints on the provenance and age of the Shuangshanzi and Qinglonghe Groups in Eastern Hebei: Implications for the tectonic evolution of the Eastern Block. Precambrian Research, 255, 699–715.

Li, Y.L., Konhauser, K.O., and Zhai, M.G. (2017) The formation of magnetite in the early Archean oceans. Earth and Planetary Science Letters, 466, 103–114.

Morris, R.C. (1993) Genetic modelling for banded iron-formation of the Hamersley Group, Pilbara Craton, Western Australia. Precambrian Research, 60(1–4), 243–286.

Mandernack, K.W., Fogel, M.L., Tebo, B.M., and Usui, A. (1995) Oxygen-isotope analyses of chemically and microbially produced manganese oxides and manganates. Geochimica et Cosmochimica Acta, 59(21), 4409–4425.

Mojzsis, S.J., Arrhenius, G., McKeegan, K.D., Harrison, T.M., Nutman, A.P., and Friend, C.R.L. (1996) Evidence for life on Earth before 3,800 million years ago. Nature, 384, 55–59.

McCollom, T.M. (2013) Laboratory simulations of abiotic hydrocarbon formation in Earth's deep subsurface. Reviews in Mineralogy and Geochemistry, 75(1), 467–494.

McDermott, J.M., Seewald, J.S., German, C.R., and Sylva, S.P. (2015) Pathways for abiotic organic synthesis at submarine hydrothermal fields. Proceedings of the National Academy of Sciences, 112(25), 7668–7672.

McMahon, S., Anderson, R.P., Saupe, E.E., and Briggs, D.E.G. (2016) Experimental evidence that

clay inhibits bacterial decomposers: Implications for preservation of organic fossils. Geology, 44(10), 867–870.

Mänd, K., Robbins, L.J., Planavsky, N.J., Bekker, A., and Konhauser, K.O. (2021) Iron Formations as Palaeoenvironmental Archives. Cambridge University Press, pp, 1–22.

Nealson, K.H., and Myers, C.R. (1990) Iron reduction by bacteria: a potential role in the genesis of banded iron formations. American Journal of Science, 290-A, 35–45.

Neumann, T., Heiser, U., Leosson, M.A., and Kersten, M. (2002) Early diagenetic processes during Mn-carbonate formation: evidence from the isotopic composition of authigenic Ca-rhodochrosites of the Baltic Sea. Geochimica et Cosmochimica Acta, 66(5), 867–879.

Nutman, A.P. (2007) Apatite recrystallisation during prograde metamorphism, Cooma, southeast Australia: implications for using an apatite–graphite association as a biotracer in ancient metasedimentary rocks. Australian Journal of Earth Sciences, 54, 1023–1032.

Nutman, A.P., Wan, Y.S., Du, L.L., Friedn, C.R.L., Dong, C.Y., Xie, H.Q., Wang, W., Sun, W., and Liu, D.Y. (2011) Multistage late Neoarchean crustal evolution of the North China Craton, eastern Hebei. Precambrian Research, 189(1–2), 43–65.

Nie, N.X., Dauphas, N., and Greenwood, R.C. (2017) Iron and oxygen isotope fractionation during iron UV photo-oxidation: implications for early Earth and Mars. Earth and Planetary Science Letters, 458, 179–191.

Nan, J.B., King, H.E., Delen, G., Meirer, F., Weckhuysen, B.M., Guo, Z.X., Peng, X.T., and Plümper, O. (2021) The nanogeochemistry of abiotic carbonaceous matter in serpentinites from the Yap Trench, western Pacific Ocean. Geology, 49(3), 330–334.

Ohtomo, Y., Kakegawa, T., Ishida, A., Nagase, T., and Rosing, M.T. (2014) Evidence for biogenic graphite in early Archaean Isua metasedimentary rocks. Nature Geoscience, 7, 25–28.

Perry Jr, E.C., and Ahmad, S.N. (1977) Carbon isotope composition of graphite and carbonate minerals from 3.8-AE metamorphosed sediments, Isukasia, Greenland. Earth and Planetary Science Letters, 36(2), 280–284.

Posth, N.R., Hegler, F., Konhauser, K.O., and Kappler, A. (2008) Alternating Si and Fe deposition caused by temperature fluctuations in Precambrian oceans. Nature Geoscience, 1, 703–708.

Pecoits, E., Smith, M.L., Catling, D.C., Philippot, P., Kappler, A., and Konhauser, K.O. (2015) Atmospheric hydrogen peroxide and Eoarchean iron formations. Geobiology, 13, 1–14.

Planavsky, N., Rouxel, O., Bekker, A., Shapiro, R., Fralick, P., and Knudsen, A. (2009) Iron oxidizing microbial ecosystems thrived in late Paleoproterozoic redox-stratified oceans. Earth and Planetary Science Letters, 286(1–2), 230–242.

Posth, N.R., Huelin, S., Konhauser, K.O., and Kappler, A. (2010) Size, density and composition of cell-mineral aggregates formed during anoxygenic phototrophic Fe(II) oxidation: impact on modern and ancient environments. Geochimica et Cosmochimica Acta, 74(12), 3476–3493.

Papineau, D., De Gregorio, B.T., Cody, G.D., O'Neil, Steele, A., Stroud, R.M., and Fogel, M.L. (2011) Young poorly crystalline graphite in the > 3.8-Gyr-old Nuvvuagittuq banded iron formation. Nature Geoscience, 4, 376–379.

Percak-Dennett, E.M., Beard, B.L., Xu, H., Johnson, C.M., and Roden, E.E. (2011) Iron isotope fractionation during microbial dissimilatory iron oxide reduction in simulated Archaean seawater. Geobiology, 9, 205–220.

Pecoits, E., Smith, M.L., Catling, D.C., Philippot, P., Kappler, A., and Konhauser, K.O. (2015) Atmospheric hydrogen peroxide and Eoarchean iron formations. Geobiology, 13, 1–14.

Papineau, D., De Gregorio, B., Fearn, S., Kilcoyne, D., McMahon, G., Purohit, R., Fogel, M. (2016) Nanoscale petrographic and geochemical insights on the origin of the Palaeoproterozoic stromatolitic phosphorites from Aravalli Supergroup, India. Geobiology, 14(1), 3–32.

Playter, T, Konhauser, K, Owttrim, G, Hodgson, C., Warchola, T., Mloszewska, A.M., Sutherland, B., Bekker, A., Zonneveld, Z.P., Pemberton, S.G., and Gingras, M. (2017) Microbe-clay interactions as a mechanism for the preservation of organic matter and trace metal biosignatures in black shales. Chemical Geology, 459, 75–90.

Planavsky, N.J., Crowe, S.A., Fakhraee, M., Beaty, B., Reinhard, C.T., Mills, B.J.W., Holstege, C., and Konhauser, K.O. (2021) Evolution of the structure and impact of Earth's biosphere[J]. Nature Reviews Earth & Environment, 2, 123–139.

Qian, X.L., Cui, W.Y., Wang, S.Q., and Wang, G.Y. (1985) Geology of Precambrian Iron Ores in Eastern Hebei Province, China. Hebei Science and Technology Press, Shijiazhuang (in Chinese).

Ruttenberg, K.C., and Berner, R. (1993) Authigenic apatite formation and burial in sediments from non-upwelling, continental margin environments. Geochimica et Cosmochimica Acta, 57(5), 991–1007.

Roden, E.E. (2003) Fe (III) oxide reactivity toward biological versus chemical reduction.

Environmental Science & Technology, 37(7), 1319–1324.

Roh, Y., Zhang, C.L., Vali, H., Lauf, R.J., Zhou, J., and Phelps, T.J. (2003) Biogeochemical and environmental factors in Fe biomineralization: magnetite and siderite formation. Clays and Clay Minerals, 51(1), 83–95.

Rasmussen, B., Fletcher, I.R., Brocks, J.J., and Kilburn, M.R. (2008) Reassessing the first appearance of eukaryotes and cyanobacteria. Nature, 455, 1101–1104.

Rasmussen, B., Krapež, B., and Meier, D.B. (2014) Replacement origin for hematite in 2.5 Ga banded iron formation: evidence for postdepositional oxidation of iron-bearing minerals. GSA Bulletin, 126(3–4), 438–446.

Rasmussen, B., Krapež, B., Muhling, J.R., and Suvorova, A. (2015) Precipitation of iron silicate nanoparticles in early Precambrian oceans marks Earth's first iron age. Geology, 43(4), 303–306.

Rasmussen, B., Muhling, J.R., Suvorova, A., and Krapež, B. (2016) Dust to dust: evidence for the formation of "primary" hematite dust in banded iron formations via oxidation of iron silicate nanoparticles. Precambrian Research, 284, 49–63.

Rasmussen, B., Muhling, J.R., Suvorova, A., and Krapež, B. (2017) Greenalite precipitation linked to the deposition of banded iron formations downslope from a late Archean carbonate platform. Precambrian Research, 290, 49–62.

Rasmussen, B, Muhling, J.R., Suvorova, A., and Fischer, W.W. (2021) Apatite nanoparticles in 3.46–2.46 Ga iron formations: Evidence for phosphorus-rich hydrothermal plumes on early Earth. Geology, 49(6), 647–651.

Reinhard, C.T., Planavsky, N.J., Gill, B.C., Ozaki, K., Robbins, L.J., Lyons, T.W., Fischer, W.W., Wang, C., Cole, D.B., and Konhauser, K.O. (2017) Evolution of the global phosphorus cycle. Nature, 541, 386–389.

Siever, R. (1992) The silica cycle in the Precambrian. Geochimica et Cosmochimica Acta, 56, 3265–3272.

Slomp, C.P., and Van Raaphorst, W. (1993) Phosphate adsorption in oxidized marine sediments. Chemical Geology, 107(3-4), 477–480.

Shanks III, W.C., Bohlke, J.K., and Seal, R.R. (1995) Stable isotopes: Tracers of interactions between fluids, minerals, and organisms. In: Humphris, S., Lupton, J., Mullineaux, L., and Zierenberg, R. (Eds.), Physical, Chemical, Biological and Geological Interactions Within

Submarine Hydrothermal Systems, Geophysical Monograph. American Geophysical Union, Washington, pp. 194–221.

Sverjensky, D.A., and Sahai, N. (1996) Theoretical prediction of single-site surface-protonation equilibrium constants for oxides and silicates in water. Geochimica et Cosmochimica Acta, 60(20), 3773–3797.

Shanks III, W.C. (2001) Stable isotopes in seafloor hydrothermal systems: vent fluids, hydrothermal deposits, hydrothermal alteration, and microbial processes. Reviews in Mineralogy and Geochemistry, 43(1), 469–525.

Slomp, C.P., Van der Gaast, S.J., and Van Raaphorst, W. (1996) Phosphorus binding by poorly crystalline iron oxides in North Sea sediments. Marine Chemistry, 52(1), 55–73.

Strauss, H. (2003) Sulphur isotopes and the early Archaean sulphur cycle. Precambrian Research, 126(3–4), 349–361.

Shen, B.F., Yang, C.L., Li, J.J., Zhai, A.M., and Zuo, Y.C. (2005) New evidence for dating the Zhuzhangzi group of Eastern Hebei. Journal of Stratigraphy, 29, 433–436 (in Chinese with English abstract).

Sun, H.Y., Dong, C.Y., Xie, H.Q., Wang, W., Ma, M.Z., Liu, D.Y., Nutman, A., and Wan, Y.S. (2010) The formation age of the Neoarchean Zhuzhangzi and Dantazi Groups in the Qinglong area, eastern Hebei province: evidence from SHRIMP U-Pb zircon dating. Geology Reviews, 56(6), 888–898 (in Chinese with English abstract).

Scott, C., Planavsky, N.J., Dupont, C.L., Kendall, B., Gill, B.C., Robbins, L.J., Husband, K.F., Arnold, G.L., Wing, B.A., Poulton, S.W., Bekker, A., Anbar, A.D., Konhauser, K.O., and Lyons, T. W. (2013) Bioavailability of zinc in marine systems through time. Nature Geoscience, 6(2), 125–128.

She, Z.B., Strother, P., and Papineau, D. (2014) Terminal Proterozoic cyanobacterial blooms and phosphogenesis documented by the Doushantuo granular phosphorites, II: microbial diversity and C isotopes. Precambrian Research, 251, 62–79.

Trendall, A.F. (1983) The Hamersley Basin. Developments in Precambrian Geology, 6, 69–129.

Trendall, A.F. (2002) The significance of iron-formation in the Precambrian stratigraphic record. International Association of Sedimentologists Special Publication, 33, 33–66.

Tosca, N.J., Guggenheim, S., and Pufahl, P.K. (2016) An authigenic origin for Precambrian

greenalite: implications for iron formation and the chemistry of ancient seawater. GSA Bulletin, 128(3–4), 511–530.

Thompson, K.J., Kenward, P.A., Bauer, K.W., Warchola, T., Gauger, T., Martinez, R., Simister, R.L., Michiels, C.C., Llirós, M., Reinhard, C.T., Kappler, A., Konhauser, K.O., and Crowe, A.S. (2019) Photoferrotrophy, deposition of banded iron formations, and methane production in Archean oceans. Science advances, 5, eaav2869.

Tong, X.X., Mänd, K., Li, Y.H., Zhang, L.C., Peng, Z.D., Wu, Q., Li, P.B., Zhai, M.G., Robbins, L.J., Wang, C.L., and Konhauser, K.O. (2021) Iron and Carbon Isotope Constraints on the Formation Pathway of Iron-Rich Carbonates within the Dagushan Iron Formation, North China Craton. Minerals, 11(1), 94.

Van Cappellen, P., and Ingall, E.D. (1994) Benthic phosphorus regeneration, net primary production, and ocean anoxia: a model of the coupled marine biogeochemical cycles of carbon and phosphorus. Paleoceanography, 9(5), 677–692.

Van Zuilen, M.A., Lepland, A., and Arrhenius, G. (2002) Reassessing the evidence for the earliest traces of life. Nature, 418, 627–630.

Walker, J.C.G. (1987) Was the Archaean biosphere upside down? Nature, 329, 710–712.

Wilde, S.A., Valley, J.W., Kita, N.T., Cavosie, A.J., and Liu, D.Y. (2008) SHRIMP U–Pb and CAMECA 1280 oxygen isotope results from ancient detrital zircons in the Caozhuang quartzite, Eastern Hebei, North China Craton: evidence for crustal reworking 3.8 Ga ago. American Journal of Science, 308(3), 185–199.

Wan, Y.S., Dong, C.Y., Liu, D.Y., Kröner, A., Yang, C.H., Wang, W., Du, L.L., Xie, H.Q., and Ma, M.Z. (2012) Zircon ages and geochemistry of late Neoarchean syenogranites in the North China Craton: a review. Precambrian Research, 222–223, 265–289.

Xiong, Y.J., Guilbaud, R., Peacock, C.L., Cox, R.P., Canfield, D.E., Krom, M.D., and Poulton, S.W. (2019) Phosphorus cycling in Lake Cadagno, Switzerland: A low sulfate euxinic ocean analogue. Geochimica et Cosmochimica Acta, 251, 116–135.

Yang, X.Q., Zhang, Z.H., Duan, S.G., and Zhao, X.M. (2015) Petrological and geochemical features of the Jingtieshan banded iron formation (BIF): A unique type of BIF from the Northern Qilian Orogenic Belt, NW China. Journal of Asian Earth Sciences, 113, 1218–1234.

Zhang, Y.X., Ye, T.S., Yan, H.S., Zheng, S.Y., Duan, C.Q., Chen, M.R., and Zhao, W.H. (1986) The

Archean Geology and Banded Iron Formation of Jidong, Hebei Province. Geological Publishing House, Beijing (in Chinese).

Zhao, G.C., Wilde, S.A., Cawood, P.A., and Lu, L. (1998) Thermal evolution of Archean basement rocks from the eastern part of the North China Craton and its bearing on tectonic setting. International Geology Review, 40(8), 706–721.

Zhao, G.C., Sun, M., Wilde, S.A., Li, S.Z. (2005) Late Archean to Paleoproterozoic evolution of the North China craton: key issues revisited. Precambrian Research, 136, 177–202.

Zegeye, A., Bonneville, S., Benning, L.G., Sturm, A., Fowle, D.A., Jones, C., Canfield, D.E., Ruby, C., MacLean, L.C., Nomosatryo, S., Crowe, S.A., and Poulton, S. W. (2012). Green rust formation controls nutrient availability in a ferruginous water column. Geology, 40(7), 599–602.

Figure Captions

FIGURE 1. Simplified geological map of Eastern Hebei indicating the study area (after Nutman et al., 2011). Insert shows the subdivisions of the North China Craton (NCC) and the location of Eastern Hebei (after Zhao et al., 2005). Stars represent typical BIFs in this area.

FIGURE 2. Simplified stratigraphic column of the Zhalanzhangzi BIF logged from drill cores Zk1103 and Zk1104. Sample locations (shown as arrows) and pictures of representative BIF samples are also provided.

FIGURE 3. Petrographic images showing mineral compositions and the distribution of graphite in the Zhalanzhangzi BIF samples. (**a**) Transmitted light image of the BIF, showing the contract between the iron- and silica-rich bands. (**b**) Cross-polar image of the iron-rich band of BIF, with networks of grunerite crystals distributing alongside the magnetite and quartz interface. (**c**) Transmitted light image of a siderite-rich network in an iron-rich band of the BIF. (**d**) Reflected light image of the boxed area in (**c**), showing the presence of graphite within siderite, as well as associated with magnetite and pyrite. (**e**) Reflected light image of an iron-rich band, with the co-occurrence of magnetite, grunerite, and graphite. (**f**) Reflected light image of a silica-rich band, showing the presence of graphite in association with pyrite and calcite. (**g–j**) Scanning electron (left) and energy dispersive X-ray (right) spectroscopy images showing the presence of graphite within and/or associated with different mineral phases in the BIF samples. Abbreviations: Sid = siderite, Bru = brunsvigite, Qz = quartz, Gru = grunerite, Cal = calcite, Alm = almandine, Mag = magnetite, Cum = cummingtonite, Gr = graphite.

FIGURE 4. Images showing the mineral components, distributions and weight percent according to scanning electron microscopy based automated mineralogy analysis on three representative BIF samples with different total organic carbon contents.

FIGURE 5. (**a**) Scanning electron (first) and energy dispersive X-ray spectroscopy images of the unexposed, fresh surface of a rock fragment from sample 1104d, showing the intergrowth of fine-grained graphite and apatite. (**b**) Scanning electron spectroscopy image of the boxed area in (**a**), showing the co-occurrence of graphite with an

apatite rosette. (c) Representative Raman spectra for the graphite and apatite in this figure. Abbreviations: Gru = grunerite, Mag = magnetite, Py = pyrite, Gr = graphite.

FIGURE 6. (**a**) Representative Raman spectra for the random analyses on graphite grains from the BIF samples and the epoxy (at variable power levels) used to fix the BIFs. (**b**) Binned frequency histogram showing crystallization temperatures computed according to the Raman analyses on the crystalline graphite from the BIF samples.

FIGURE 7. (**a**) Scanning electron spectroscopy image showing the close association of graphite with apatite in the iron-rich band. (**b**) Scanning electron (left) and energy dispersive X-ray (right) spectroscopy images showing the co-occurrence of graphite and chlorite in the silica-rich band. (**c**) Representative Raman spectra for the interested area (left, reflected light), revealing the presence of graphite within grunerite and feldspar grains. (**d**) Reflected light (left) and Raman spectra (right) images showing the presence of graphite inclusions in apatite grain. Abbreviations: Qz = quartz, Ap = apatite, Mt = magnetite, Gr = graphite, Ank = ankerite, Py = pyrite, Chl = chlorite, Gru = grunerite, Fsp = feldspar.

FIGURE 8. (**a**) Scanning electron spectroscopy image showing that graphite is unevenly distributed in the iron- and silica-rich bands. (**b**) Scanning electron spectroscopy image of the boxed area in (**a**), showing the distribution of graphite in iron-rich bands. (**c–e**) Reflected light images showing the close associations of graphite with magnetite, siderite and pyrite. (**f**) Scanning electron spectroscopy image showing the replacement of siderite by coarse-grained calcite and existence of siderite relict edges in coarser calcite grains. (**g**) Scanning electron (upper) and energy dispersive X-ray (lower) images showing that anhedral to sub-spherical graphite grains were sealed in coarse-grained quartz. (**h**) Representative Raman spectra for this figure. Abbreviations: Qz = quartz, Sid = siderite, Py = pyrite, Mt = magnetite, Gr = graphite, Gru = grunerite, Cal = calcite, Chl = chlorite, Ap = apatite.

Table Captions

TABLE 1. Mineral association (expressed as % association) of graphite with other minerals in the Zhalanzhangzi BIF, computed by SEM-AM analysis.

TABLE 2. Major oxides, total inorganic and organic carbon contents, and carbon isotope values for the Zhalanzhangzi BIF.

Supplemental Material

FIGURE S1. Simplified geological map of the Zhalanzhangzi BIF showing the geologic context of the study area and locations of the two drill cores.

FIGURE S2. Cross-plot for selected data in the Zhalanzhangzi BIF. The inset shows the correlation between TOC and Al_2O_3 excluding the two samples with high Al_2O_3 contents.

FIGURE S3. (**a**) Scanning electron (left) and energy dispersive X-ray (right) spectroscopy images showing the close

association of magnetite with the co-occurrence of apatite and graphite. (**b**) Scanning electron (first) and energy dispersive X-ray spectroscopy images of the boxed area in (**a**), showing the presence of fine-grained graphite inclusions within apatite. Abbreviations: Gru = grunerite, Qz = quartz, Mag = magnetite, Gr = graphite, Ap = apatite.

TABLE S1. Electron probe microanalysis of minerals in the Zhalanzhangzi BIF.

TABLE S2. Geological reference materials used in this study with recommended and measured values.

TABLE S3. Raman spectral parameters and crystallization temperature estimates (Beyssac et al., 2003) for graphitic carbon in the Zhalanzhangzi BIF.

TABLE S4. Calculation of primary organic carbon.

TABLE 1. Mineral association (expressed as % association) of graphite with other minerals in the Zhalanzhangzi BIF, computed by SEM-AM analysis.

Sample 1103b														
Minerals	Graphite	Quartz	Calcite	Ankerite	Pyrite	Magnetite	Siderite	Grunerite	Actinolite	Apatite	Feldspar	Chlorite	Cummingtonite	Else
Graphite	0.0	54.2	3.3	3.1	2.5	4.2	9.7	3.8	1.0	0.8	6.4	7.7	0.1	3.1
Quartz	3.0	0.0	4.8	1.6	2.7	1.6	21.0	13.8	6.6	1.4	22.4	14.9	0.5	3.5
Calcite	2.2	57.1	0.0	9.3	0.2	0.6	8.9	6.2	0.2	0.1	1.2	4.4	0.0	8.7
Ankerite	3.1	28.1	14.3	0.0	1.1	0.7	21.2	9.9	0.3	0.8	3.8	9.2	0.0	5.8
Pyrite	2.5	47.8	0.3	1.1	0.0	2.8	21.9	2.7	0.1	0.3	2.6	4.6	0.0	12.8
Magnetite	4.4	29.4	0.9	0.7	2.9	0.0	36.0	15.6	0.1	0.4	0.8	3.5	0.0	4.2
Siderite	0.8	30.5	1.1	1.7	1.8	2.8	0.0	23.6	0.5	1.7	5.4	28.1	0.2	1.3
Grunerite	0.5	31.3	1.2	1.2	0.3	1.9	36.7	0.0	0.6	0.8	3.7	20.4	0.1	1.0
Actinolite	0.3	39.1	0.1	0.1	0.0	0.0	2.0	1.7	0.0	2.6	27.9	21.3	2.4	2.1
Apatite	0.9	27.9	0.1	0.9	0.4	0.4	22.2	6.7	8.6	0.0	9.9	15.3	0.0	6.3
Feldspar	0.7	45.0	0.2	0.4	0.3	0.1	7.4	3.3	9.5	1.0	0.0	28.0	1.8	1.4
Chlorite	0.7	23.0	0.6	0.8	0.4	0.3	29.8	13.9	5.5	1.2	21.5	0.0	0.8	1.3
Cummingtonite	0.1	19.5	0.1	0.0	0.0	0.0	5.1	1.4	16.0	0.1	35.6	19.8	0.0	2.1
Else	1.9	37.9	7.8	3.4	7.6	2.4	9.8	4.9	3.8	3.5	7.4	8.9	0.6	0.0
Sample 1104b														
Graphite	0.0	28.4	0.6		0.4	1.7	2.5	3.3	0.8	1.6		50.8		9.5
Quartz	16.4	0.0	6.2		4.3	9.0	7.3	19.0	0.2	0.8		17.4		11.7
Calcite	2.2	37.3	0.0		0.3	1.5	5.3	19.4	0.1	0.3		14.9		17.5
Ankerite														
Pyrite	3.1	54.0	0.6		0.0	1.1	2.0	3.8	0.3	0.0		4.9		29.7
Magnetite	3.7	35.0	1.0		0.4	0.0	5.8	25.8	0.0	3.0		12.6		10.9
Siderite	5.5	27.3	3.3		0.6	5.7	0.0	29.2	0.0	0.1		23.1		4.6
Grunerite	3.2	32.0	5.5		0.5	11.2	13.1	0.0	0.0	1.5		26.2		6.7
Actinolite	42.4	15.2	1.6		2.0	0.3	0.1	1.1	0.0	0.6		25.9		10.7
Apatite	11.0	9.6	0.6		0.0	9.4	0.2	10.7	0.1	0.0		19.8		38.5
Feldspar														
Chlorite	35.2	20.8	3.0		0.5	3.9	7.4	18.7	0.3	2.0		0.0		7.9
Cummingtonite														
Else	13.6	28.9	7.2		5.9	7.0	3.1	9.8	0.3	7.9		16.3		0.0

Sample 1104d										
Graphite	0.0	1.6	14.6	0.1	8.7	59.9	1.5	2.9	1.0	9.7
Quartz	0.8	0.0	3.7	0.0	14.1	67.4	0.4	0.2	2.0	9.8
Calcite	6.3	3.4	0.0	0.0	10.0	35.4	16.3	1.0	0.5	25.6
Ankerite										
Pyrite	2.0	1.6	1.8	0.0	44.8	23.3	0.5	0.0	0.8	22.3
Magnetite	1.5	5.3	4.0	0.3	0.0	52.5	0.6	1.0	1.3	32.5
Grunerite	6.7	16.4	9.2	0.1	34.0	0.0	6.5	2.2	5.0	17.8
Actlinolite	1.3	0.8	32.3	0.0	2.9	49.9	0.0	1.9	1.2	9.7
Apatite	7.0	1.2	5.6	0.0	13.8	47.5	5.3	0.0	0.1	19.2
Feldspar										
Chlorite										
Cummingtonite	1.5	6.5	1.6	0.0	11.4	66.5	2.1	0.1	0.0	7.9
Else	2.1	4.6	12.8	0.2	40.5	34.4	2.5	1.7	1.1	0.0

Note: The colour gradients of the table highlight the most prominent association of graphite with other minerals, while the blanks show the minerals that were not detected. EPMA analysis indicates the composition of chlorite is brunsvigite, see Table S1 for details.

TABLE 2. Major oxides, total inorganic and organic carbon contents, and carbon isotope values for the Zhalanzhangzi BIF.

Sample	1103a	1103b	1103c	1103d	1103e	1103f	1103g	1103h	1104a	1104b	1104c	1104d	1104f	1104g	1104h
wt%															
SiO_2	58.4	82.6	58.2	72.4	53.6	52.0	55.7	58.2	38.3	67.4	44.0	42.5	30.2	44.3	64.2
TiO_2	0.02	0.01	0.09	0.01	0.02	0.10	0.03	0.02	0.03	0.02	0.02	0.01	0.02	0.03	0.01
Al_2O_3	0.58	0.06	4.42	0.40	0.86	3.68	0.66	0.74	1.17	1.03	0.87	0.56	0.88	1.19	0.19
Fe_2O_3	32.7	12.9	24.2	20.2	38.1	34.2	36.8	34.8	50.0	18.2	45.2	47.6	54.0	43.4	31.7
MnO	0.15	0.10	0.33	0.13	0.22	0.39	0.24	0.14	0.16	0.26	0.12	0.15	0.23	0.16	0.12
MgO	2.03	0.90	1.53	1.43	2.96	2.39	2.61	2.51	2.65	1.33	2.37	2.68	4.31	2.71	1.43
CaO	3.63	1.24	2.29	2.35	2.22	2.52	2.37	1.02	4.32	4.00	4.13	3.33	4.87	4.69	0.74
Na_2O	0.01	0.01	0.01	0.01	0.03	0.03	0.01	0.03	0.01	0.01	0.07	0.03	0.03	0.09	0.00
K_2O	0.02	0.01	0.86	0.07	0.05	0.82	0.01	0.03	0.01	0.01	0.06	0.01	0.06	0.03	0.01
P_2O_5	0.10	0.01	0.14	0.09	0.16	0.14	0.17	0.17	0.23	0.12	0.17	0.20	0.13	0.14	0.03
SO_3	0.77	1.03	1.64	0.64	0.17	1.80	0.52	0.73	1.16	0.82	0.73	0.35	1.65	0.93	0.71
LOI	1.57	0.77	6.16	2.19	1.09	1.82	0.70	0.82	1.57	6.20	1.71	2.07	3.36	2.05	0.80
Total	100.0	99.6	99.9	99.9	99.4	99.9	99.8	99.2	99.5	99.3	99.5	99.4	99.7	99.7	100.0
TIC	1.32	1.26	1.66	0.89	0.47	0.48	0.37	1.31	0.81	1.92	0.83	0.73	0.81	0.96	1.05
TOC	0.37	0.49	0.63	0.51	0.58	0.73	0.41	0.41	0.51	0.19	0.38	1.10	0.96	0.40	0.57
‰, VPDB															
$\delta^{18}O$	16.24	17.36	15.15	16.18	19.51	15.81	16.52	15.87	16.92	14.12	17.33	17.53	19.99	17.69	16.98
$\delta^{13}C_{carb}$	-7.65	-9.51	-6.57	-8.27	-12.52	-11.10	-12.13	-8.70	-14.53	-6.33	-16.73	-13.74	-13.35	-16.13	-9.27
$\delta^{13}C_{organic}$	-16.15	-15.36	-17.87	-17.80	-17.64	-18.86	-20.11	-19.92	-20.27	-21.38	-23.61	-20.68	-23.81	-23.21	-22.42

Figure 1

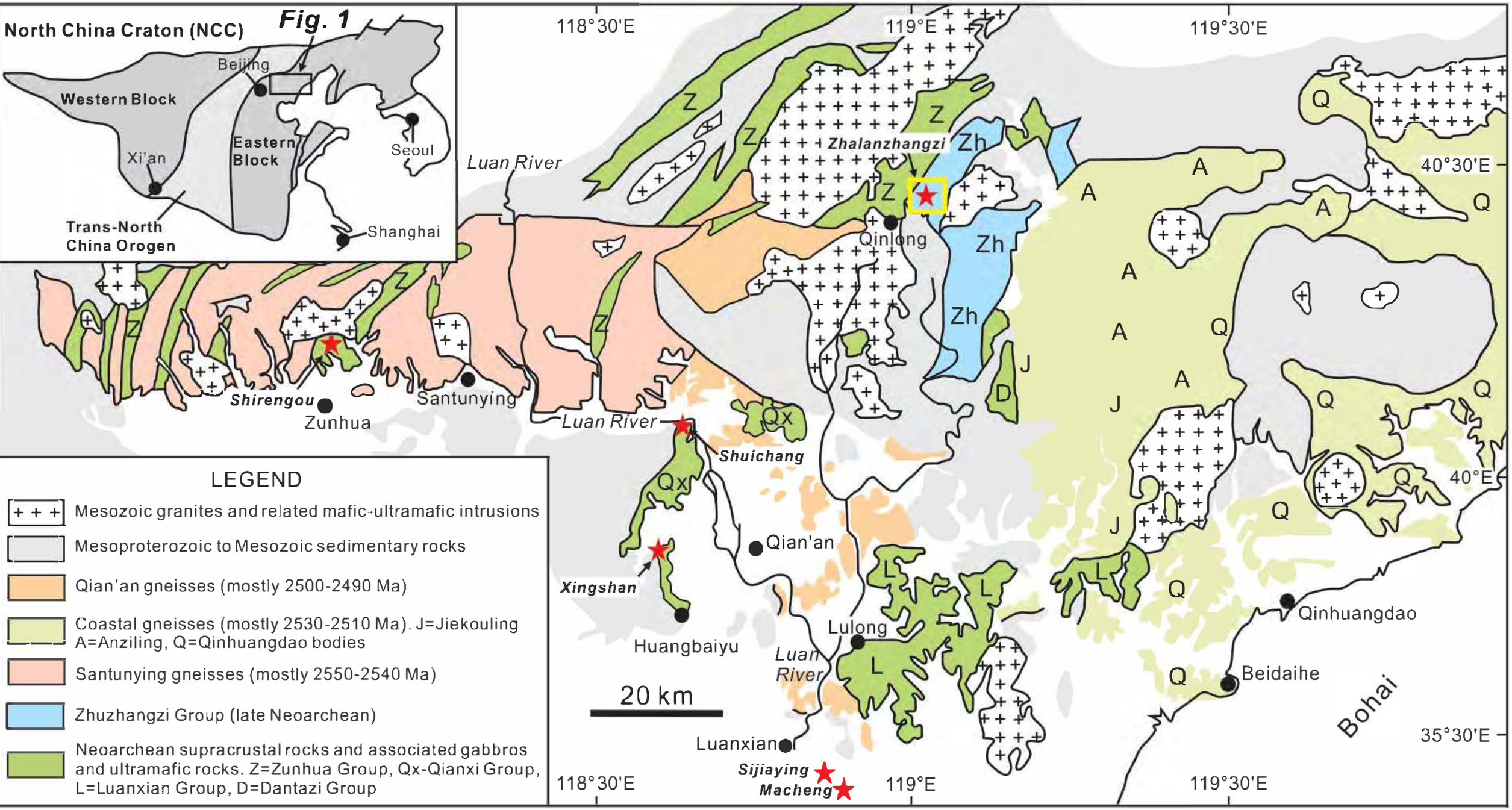
North China Craton (NCC)
Fig. 1
Beijing
Western Block
Eastern Block
Xi'an
Seoul
Trans-North China Orogen
Shanghai
118°30'E
119°E
119°30'E
40°30'E
40°E
35°30'E
Luan River
Zhalanzhangzi
Qinlong
Shirengou
Zunhua
Santunying
Shuichang
Qian'an
Xingshan
Huangbaiyu
Lulong
Luanxian
Sijiaying
Macheng
Qinhuangdao
Beidaihe
Bohai
20 km
LEGEND
Mesozoic granites and related mafic-ultramafic intrusions
Mesoproterozoic to Mesozoic sedimentary rocks
Qian'an gneisses (mostly 2500-2490 Ma)
Coastal gneisses (mostly 2530-2510 Ma). J=Jiekouling A=Anziling, Q=Qinhuangdao bodies
Santunying gneisses (mostly 2550-2540 Ma)
Zhuzhangzi Group (late Neoarchean)
Neoarchean supracrustal rocks and associated gabbros and ultramafic rocks. Z=Zunhua Group, Qx-Qianxi Group, L=Luanxian Group, D=Dantazi Group

Figure 2

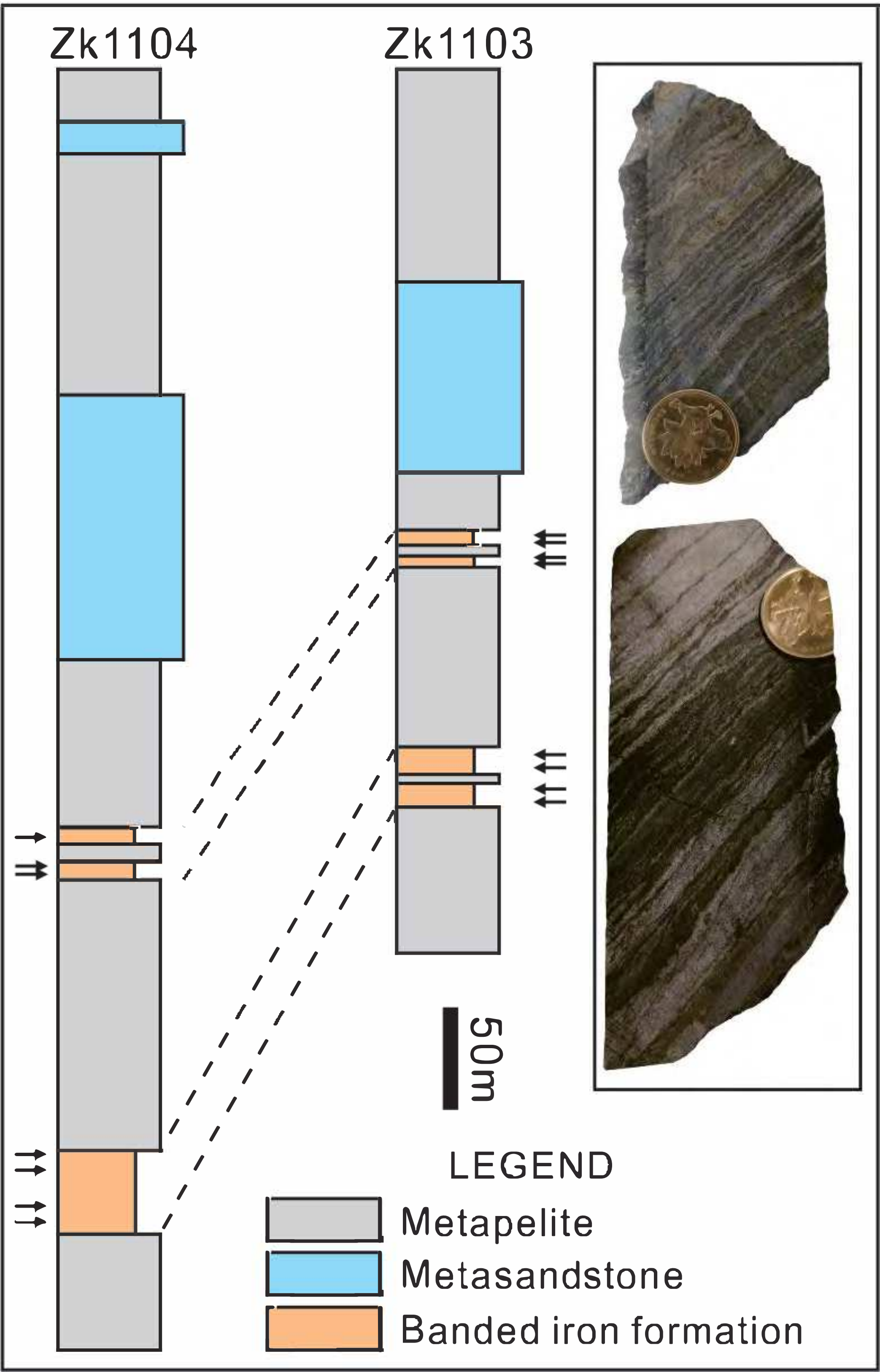
Zk1104
Zk1103
50m
LEGEND
Metapelite
Metasandstone
Banded iron formation

Figure 3

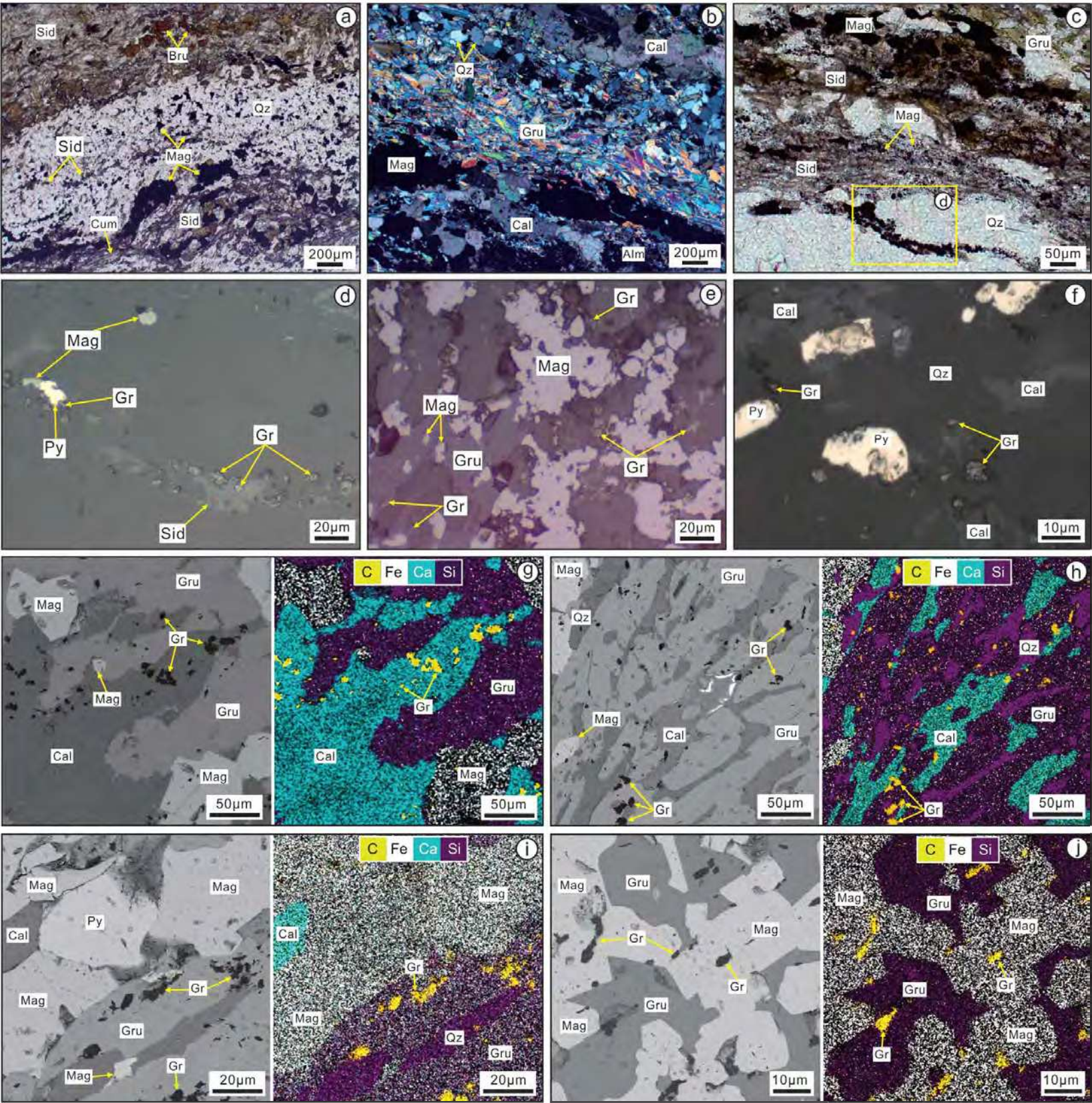
a
Sid
Bru
Qz
Sid
Mag
Cum
Sid
200μm
b
Qz
Cal
Gru
Mag
Cal
Alm
200μm
c
Mag
Gru
Sid
Mag
Sid
d
Qz
50μm
d
Mag
Gr
Py
Gr
Sid
20μm
e
Gr
Mag
Mag
Gru
Gr
Gr
20μm
f
Cal
Qz
Gr
Cal
Py
Py
Gr
Cal
10μm
Gru
Mag
Gr
Mag
Gru
Cal
Mag
50μm
C Fe Ca Si
g
Gr
Gru
Cal
Mag
50μm
Mag
Gru
Qz
Gr
Mag
Cal
Gru
Gr
50μm
C Fe Ca Si
h
Qz
Gru
Cal
Gr
50μm
Mag
Mag
Py
Cal
Gr
Mag
Gru
Mag
Gr
20μm
C Fe Ca Si
i
Mag
Cal
Gr
Mag
Qz
Gru
20μm
Mag
Gru
Mag
Gr
Gr
Gru
Mag
10μm
C Fe Si
j
Mag
Gru
Mag
Gr
Gru
Mag
Gr
10μm

Figure 4

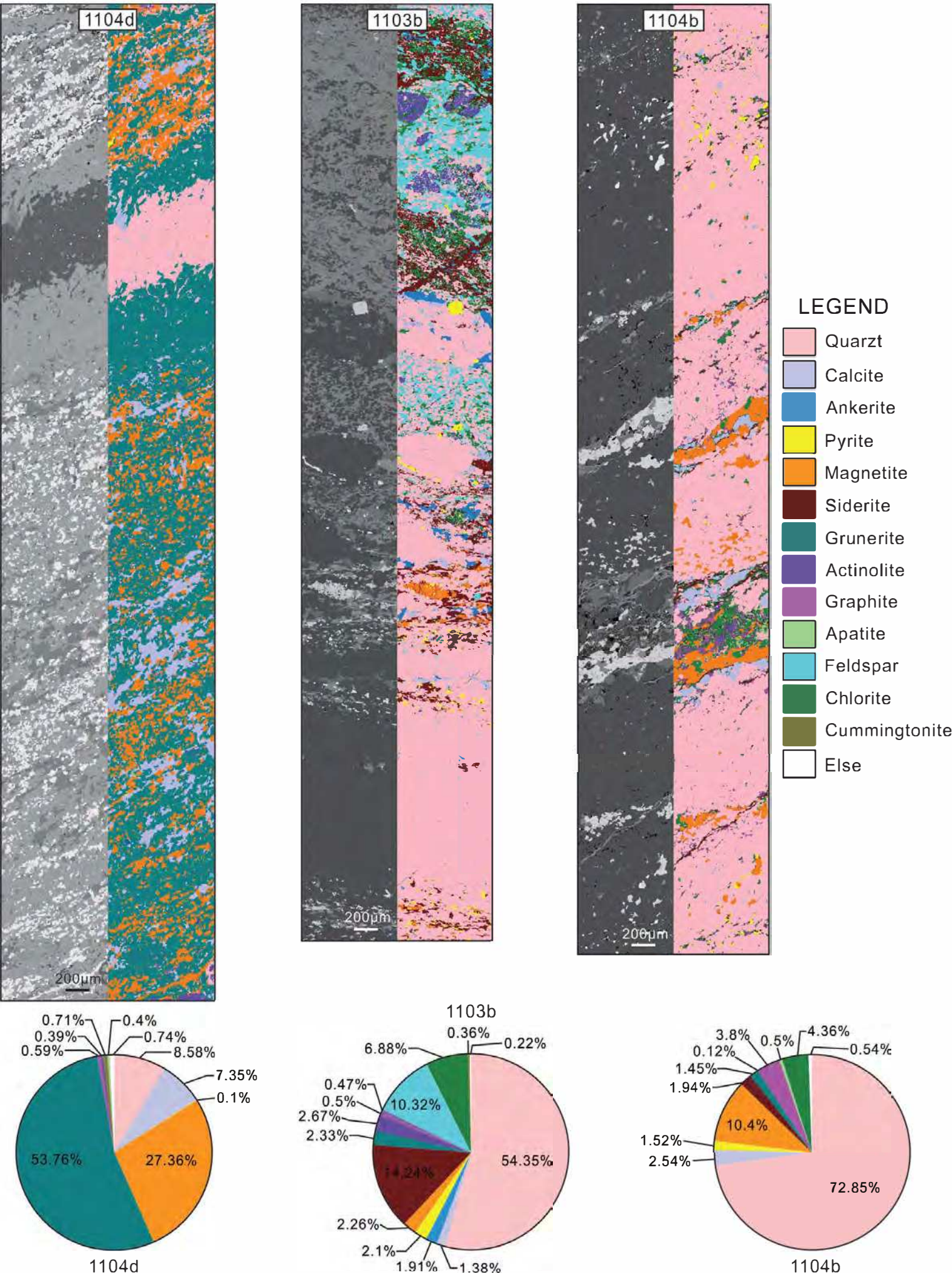
1104d
1103b
1104b
200µm
200µm
200µm
LEGEND
Quarzt
Calcite
Ankerite
Pyrite
Magnetite
Siderite
Grunerite
Actinolite
Graphite
Apatite
Feldspar
Chlorite
Cummingtonite
Else
0.71%
0.4%
0.39%
0.74%
0.59%
8.58%
7.35%
0.1%
53.76%
27.36%
1104d
1103b
0.36%
0.22%
6.88%
0.47%
0.5%
10.32%
2.67%
2.33%
14.24%
54.35%
2.26%
2.1%
1.91%
1.38%
3.8%
0.5%
4.36%
0.12%
0.54%
1.45%
1.94%
10.4%
1.52%
2.54%
72.85%
1104b

Figure 5

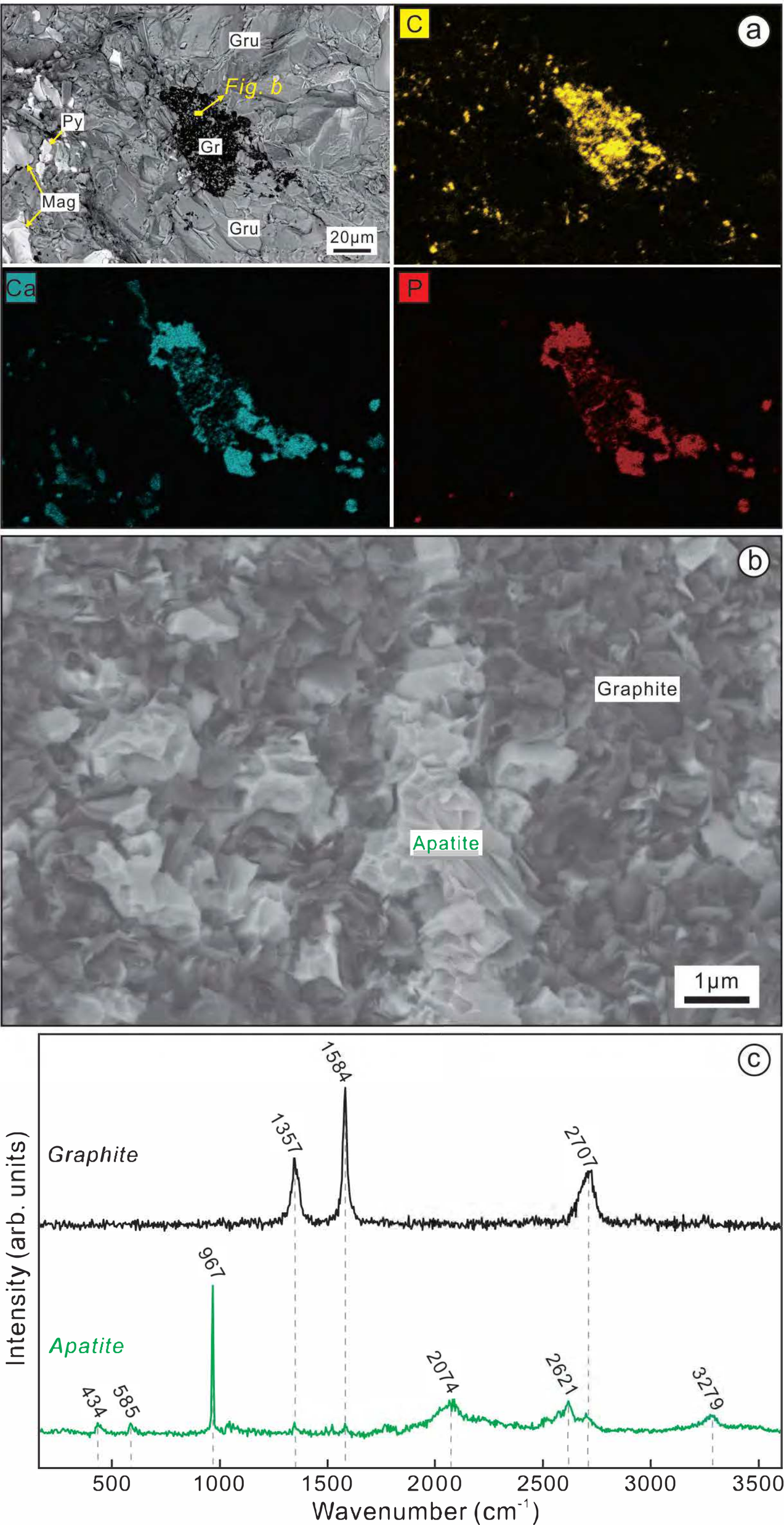
Gru
Fig. b
Py
Gr
Mag
Gru
20μm
C
a
Ca
P
b
Graphite
Apatite
1μm
c
Graphite
1357
1584
2707
Apatite
967
434
585
2074
2621
3279
Intensity (arb. units)
500
1000
1500
2000
2500
3000
3500
Wavenumber (cm-1)

Figure 6

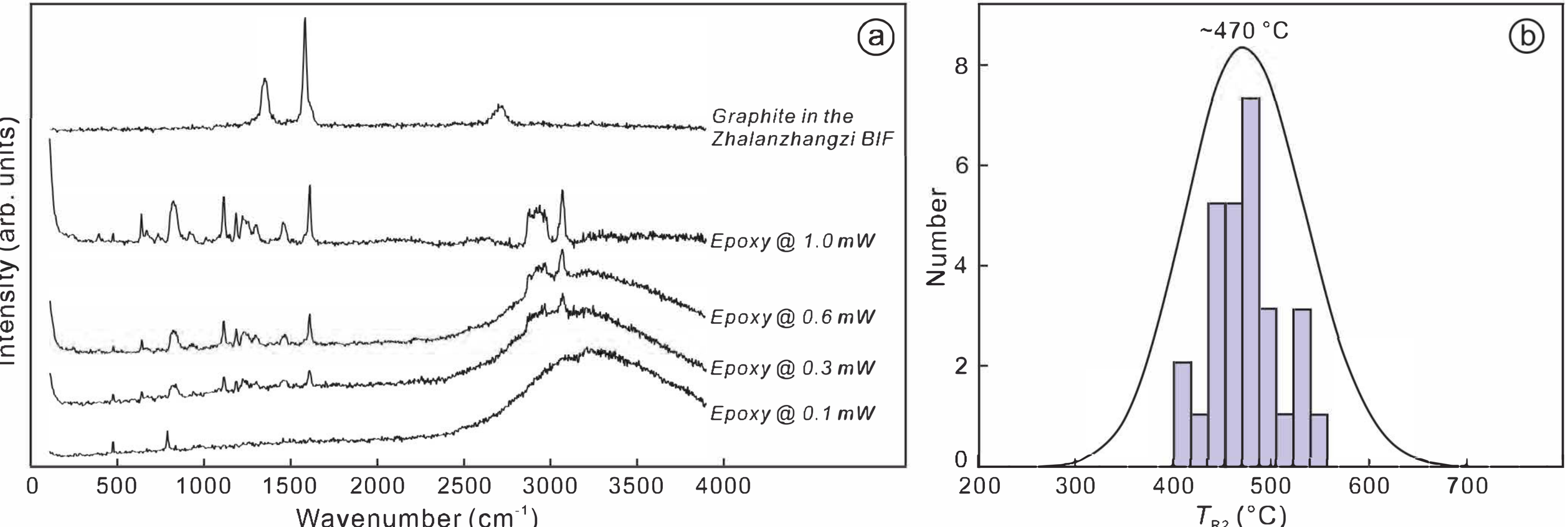
a
Graphite in the Zhalanzhangzi BIF
Epoxy @ 1.0 mW
Epoxy @ 0.6 mW
Epoxy @ 0.3 mW
Epoxy @ 0.1 mW
Intensity (arb. units)
0
500
1000
1500
2000
2500
3000
3500
4000
Wavenumber (cm-1)
b
~470 °C
Number
0
2
4
6
8
200
300
400
500
600
700
T_{R2} (°C)

Figure 7

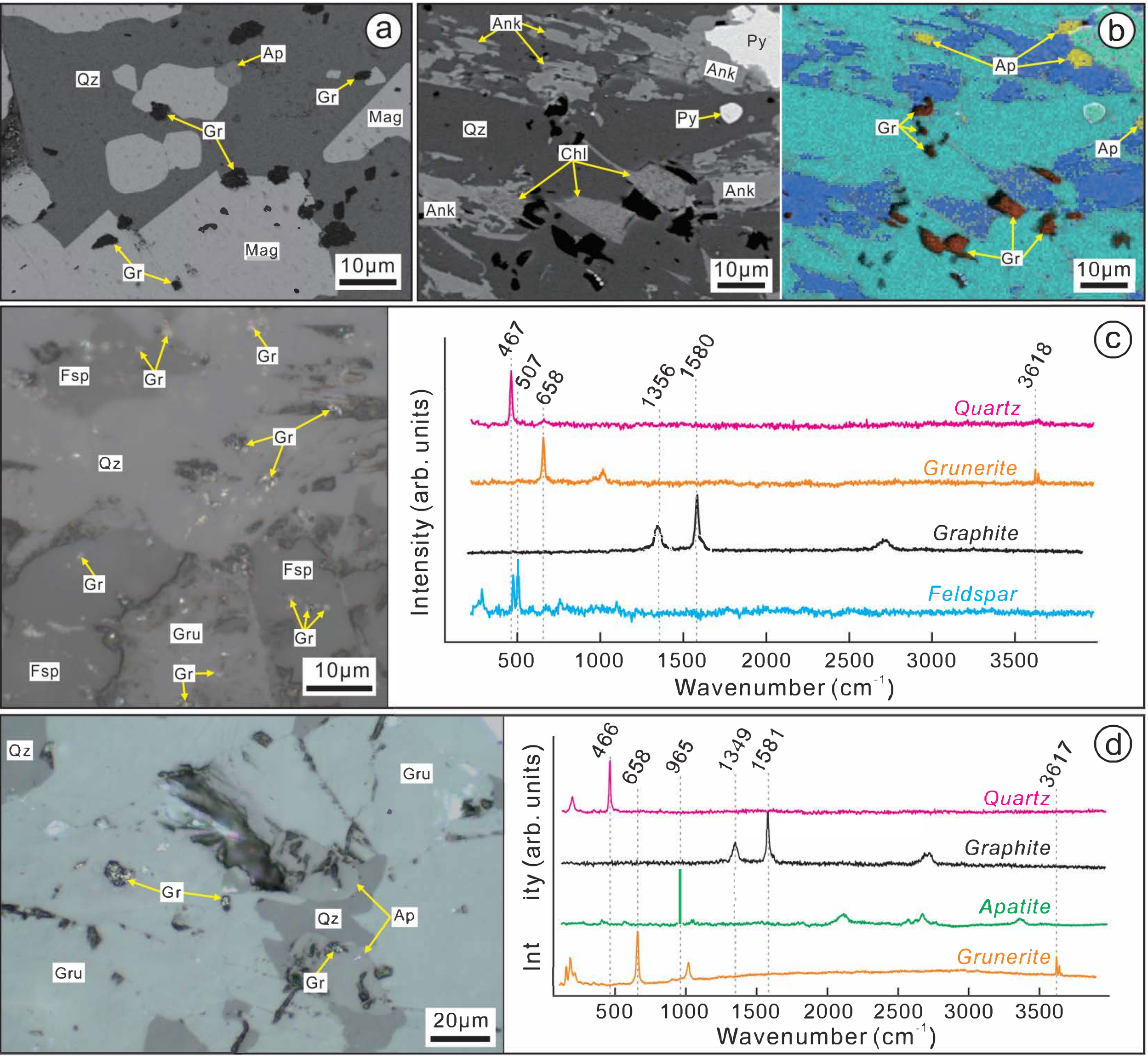
a
Qz
Ap
Gr
Gr
Mag
Mag
Gr
10μm
Ank
Py
Ank
Py
Qz
Chl
Ank
Ank
10μm
b
Ap
Gr
Ap
Gr
10μm
Fsp
Gr
Gr
Qz
Gr
Gr
Fsp
Gr
Gru
Gr
Fsp
Gr
10μm
c
467
507
658
1356
1580
3618
Quartz
Grunerite
Graphite
Feldspar
Intensity (arb. units)
500
1000
1500
2000
2500
3000
3500
Wavenumber (cm-1)
Qz
Gru
Gr
Qz
Ap
Gru
Gr
20μm
d
466
658
965
1349
1581
3617
Quartz
Graphite
Apatite
Grunerite
Int ity (arb. units)
500
1000
1500
2000
2500
3000
3500
Wavenumber (cm-1)

Figure 8

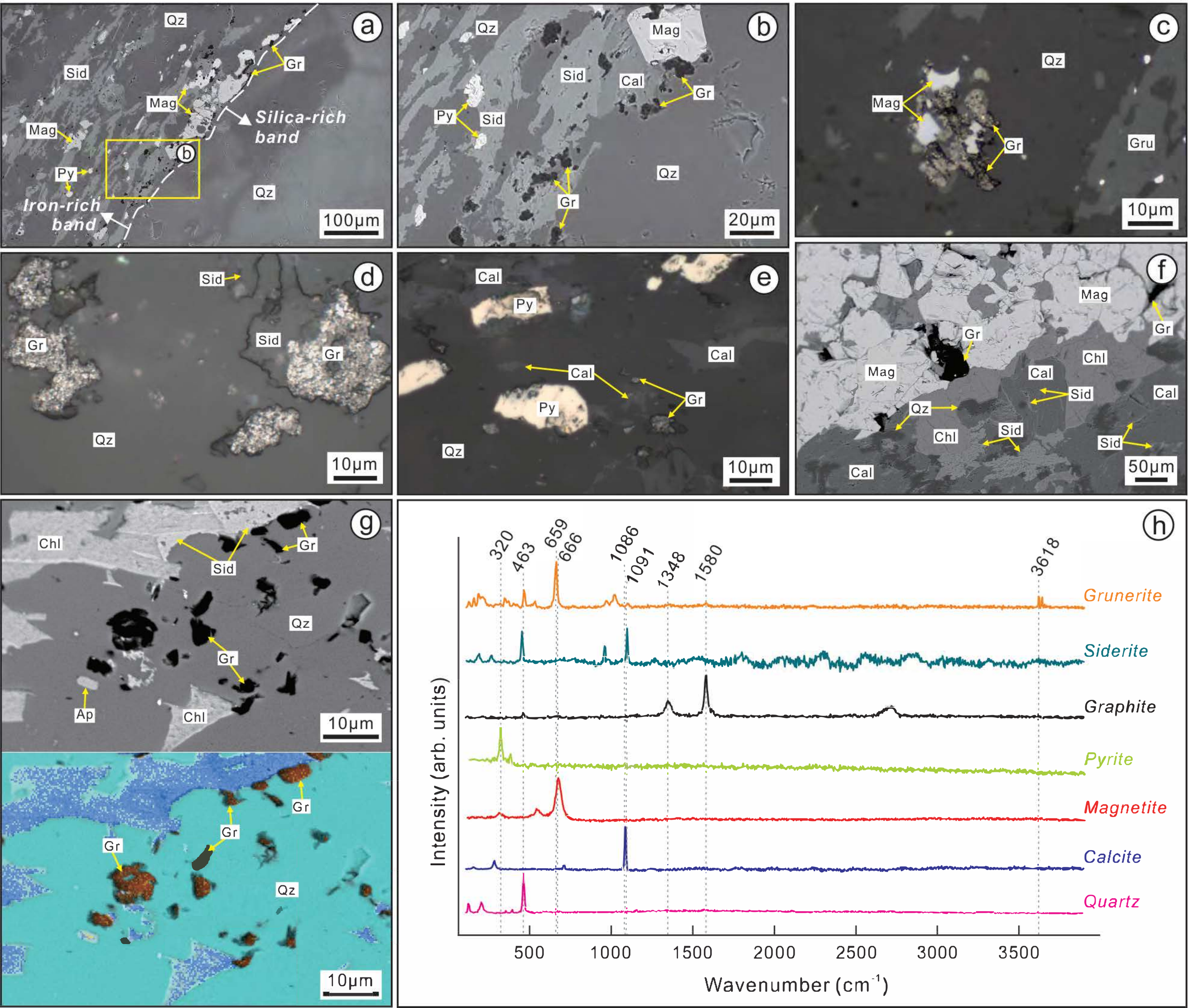
a
Qz
Sid
Gr
Mag
Silica-rich band
Mag
b
Py
Iron-rich band
Qz
100μm
b
Qz
Mag
Sid
Cal
Gr
Py
Sid
Qz
Gr
20μm
c
Qz
Mag
Gr
Gru
10μm
d
Sid
Gr
Sid
Gr
Qz
10μm
e
Cal
Py
Cal
Cal
Gr
Py
Qz
10μm
f
Mag
Gr
Gr
Chl
Mag
Cal
Sid
Cal
Qz
Chl
Sid
Sid
Cal
50μm
g
Chl
Gr
Sid
Qz
Gr
Ap
Chl
10μm
Gr
Gr
Gr
Qz
10μm
h
320
463
659
666
1086
1091
1348
1580
3618
Grunerite
Siderite
Graphite
Pyrite
Magnetite
Calcite
Quartz
Intensity (arb. units)
500
1000
1500
2000
2500
3000
3500
Wavenumber (cm-1)